X-ray photoelectron diffraction analysis of the epitaxial growth of titanium on the (110) surface of aluminum

by Volker Krasemann

A thesis submitted in partial fulfillment of the requirements of the degree of Master of Science in Physics
Montana State University
© Copyright by Volker Krasemann (1996)

Abstract:
The growth of Ti films on the Al(110) surface at room temperature has been studied using X-ray photoelectron diffraction (XPD) and low energy electron diffraction (LEED). The overlayer coverages were determined with RBS. The area under the Al 2p and the Ti 2p| 1/2 and 2p 3/2 photoelectron peaks was recorded in dependence of the polar angle.

Both LEED and XPD support an epitaxial growth of Ti on Al in form of islands. The structure of the Ti overlayer is pseudomorphic fee. A distortion of the overlayer was measured with LEED. The interlayer distance of the first two Ti overlayer is smaller than that for the bulk Al as can be concluded from a shift of the forwardscattering peak in the diffraction pattern for Ti.

A shift of the forward-scattering peak in the polar angle scan for Al indicates an expansion of the first. top layers in the Al substrate. Due to the absence of a strong forward-scattering peak in the Al scan for coverages above three monolayers the interdiffusion of bulk Al into the Ti film can be ruled out.

The Ti overlayer exhibits no long-range order for coverages of eight monolayers but still shows short-range order according to XPD.

X-RAY PHOTOELECTRON DIFFRACTION ANALYSIS OF THE EPITAXIAL GROWTH OF TITANIUM ON THE (110) SURFACE OF ALUMINUM

by

Volker Krasemann

A thesis submitted in partial fulfillment

of the requirements of the degree

of

Master of Science

in

Physics

MONTANA STATE UNIVERSITY-BOZEMAN
Bozeman, Montana

June, 1996

N378
K8648

APPROVAL

of a thesis submitted by

Volker Krasemann

This thesis has been read by each member of the thesis committee, and has been found to be satisfactory regarding content, English usage, format, citations, bibliographic style, and consistency, and is ready for submission to the College of Graduate Studies.

7-12-96 — Date

R. J. Smith — Chairperson, Graduate Committee

Approved for the Physics Department

7-12-96 — Date

Head, Physics Department

Approved for the College of Graduate Studies

7/30/96 — Date

Graduate Dean

STATEMENT OF PERMISSION TO USE

In presenting this thesis in partial fulfillment of the requirements for a master's degree at Montana State University - Bozeman, I agree that the Library shall make it available to borrowers under rules of the Library.

If I have indicated my intention to copyright this thesis by including a copyright notice page, copying is allowable only for scholarly purposes, consistent with "fair use" as prescribed in the U.S. Copyright Law. Requests for permission for extended quotation from or reproduction of this thesis in whole or in parts may be granted only by the copyright holder.

Signature 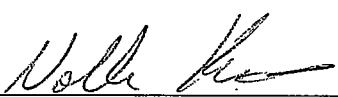

Date 07/15/96

I wish to dedicate this thesis to

David Letterman

ACKNOWLEDGMENTS

I wish to acknowledge Dr. Richard J. Smith to whom I am very thankful for his advice and guidance and for all his support not only in regards to this thesis. It was a great pleasure to be a student under Dr. Smith's supervision. I am thankful to the Physics Department, especially Dr. J. C. Hermanson for the help and financial support I received during my graduate studies at Montana State University. Also I would like to thank N. R. Shivaparan for all his collaboration and continuous assistance. My thanks go to N. Williams and E. Andersen for their technical support and assistance.

This work was supported a grant by the National Science Foundation – Grant No. NSF Grant DMR - 9409205.

TABLE OF CONTENTS

1. Introduction 1

2. Experimental Setup 3

The Ultrahigh Vacuum Chamber 3

The Accelerator and Helium High Energy Particle Detector 5

The X-ray Photoelectron Spectrometer 6

The Reverse View Low Energy Electron Diffraction Optics 8

3. Experimental Techniques 11

Sample Preparation 11

High Energy Ion Scattering 13

X-Ray Photoelectron Diffraction 15

X-Ray Photoelectron Spectroscopy 15

Experimental Design 17

Single Scattering Theory 18

Low Energy Electron Diffraction 20

4. Experimental Results for the Deposition of Ultrathin Ti Films on Al(110) 31

Rutherford Backscattering 31

X-Ray Photoelectron Diffraction 31

Curve Fitting 31

Results 34

Low Energy Electron Diffraction 41

5. Interpretation of the Results 46

X-Ray Photoelectron Diffraction Results 46

Low Energy Electron Diffraction Results 51

6. Conclusion **63**

BIBLIOGRAPHY **64**

LIST OF FIGURES

1 Schematic side view of the chamber 4
2 Schematic top view of the chamber 5
3 X-ray photoelectron spectroscopy system 7
4 Schematic diagram of the LEED optics and electrical connections . . 10
5 XPS spectrum of the Al 2p peak for (a) before sputtering and (b) after sputtering showing the clean crystal. 22
6 RBS spectrum for an 8.9 ML thick Ti overlayer on Al 23
7 XPS spectrum of Ti. The Ti 2p core-level peak is split due to spin-orbit interaction. 24
8 Geometry of the XPD experiment 25
9 Schematic representation of the XPD experiment 26
10 Scattering amplitude for an electron plane wave incident on a Cu atom at different energies [9] 27
11 Structural diagram illustrating the interplanar distortion that can be achieved by pseudomorhic growth. 28
12 Defocusing effect. The first one or two scattering events tend to be forward-focusing and subsequent events tend to be defocusing. 29
13 Relation between the LEED diffraction pattern and the reciprocal *k space* 30
14 XPS peaks for Al ($2p$) and Ti ($2p_{\frac{1}{2}}$ and $2p_{\frac{3}{2}}$). The dotted line represents the background. The peak areas after background subtraction are shown below the actual peaks. 33
15 XPD pattern for Al(110) secondary electrons. The figure shows the polar angle dependence of the background and the spline fit through the background. 35
16 *fcc* crystal direction and respective angles for the [110] and [100] azimuths 36
17 Polar angle scans of the Al 2p peak area in the [110] substrate azimuth for different coverages of Ti on Al (110) 37
18 Polar angle scans of the Al 2p peak area in the [100] substrate azimuth for different coverages of Ti on Al(110) 38
19 Polar angle scans of the Ti $2p_{\frac{1}{2}}$, $2p_{\frac{3}{2}}$ combined peak area in the [110] substrate azimuth for different coverages of Ti on Al(110) 39
20 Polar angle scans of the Ti $2p_{\frac{1}{2}}$, $2p_{\frac{3}{2}}$ combined peak area in the [100] substrate azimuth for different coverages of Ti on Al(110) 40
21 LEED patterns for Al with different coverages of Ti. (a) - (c) show the LEED patterns for energies 46.8 eV, 48.9 eV, and 46.8 eV for clean Al and two different coverages of Ti. (a) clean Al, (b) 1.9 ML of Ti on Al, (c) 5.5 ML of Ti. 42
22 LEED patterns for Al with different coverages of Ti. (a) - (d) show the spots for energies 86.2 eV, 90.4 eV, 86 eV, and 119 eV for clean Al and three different coverages of Ti. (a) clean Al, (b) 1.9 ML of Ti on Al, (c) 5.5 ML of Ti, (d) 8.1 ML of Ti. 43
23 Identification of the LEED spots for 46 eV and 86 eV and the angle between the two axis for clean Al and coverages of 1.9 ML and 5.5 ML. 45
24 Polar angle distribution of the Al $2p$ intensity for clean Al and with a coverage of 1.8 ML of Ti on Al(110) in the [110] azimuth 54
25 Polar angle distribution of the Al $2p$ intensity for Al for 4.8 ML and 8.9 ML coverages of Ti in the [110] azimuth 55

26 Polar scan for the Ti 2*p* for a coverage of 1.8 ML of Ti on Al(110) in the [110] azimuth. 56
27 Comparison between the Ti polar scan for 1.8 ML and the Al scan for clean Al in the [110] azimuth. 57
28 Polar scan for the Ti 2*p* for a coverage of 1.8, 2.5, and 4.8 ML of Ti on Al(110) in the [110] azimuth. 58
29 *fcc* lattice structure indicating a change due to strain 59
30 Polar angle scans for Al and Ti in the [110] azimuth. The diffraction pattern for Ti is taken for 8.9 ML of Ti on Al. The Al pattern is shifted to allow a better comparison. 60
31 Mechanism of the lattice distortion that can cause the observed LEED patterns. 61
32 Distortion of the LEED spots. Indicated are the changes in angles and distances. 62

LIST OF TABLES

1 Deposition Parameters and resulting thicknesses 32
2 Angles and distances for LEED spots 44

ABSTRACT

The growth of Ti films on the Al(110) surface at room temperature has been studied using X-ray photoelectron diffraction (XPD) and low energy electron diffraction (LEED). The overlayer coverages were determined with RBS. The area under the Al $2p$ and the Ti $2p\frac{1}{2}$ and $2p\frac{3}{2}$ photoelectron peaks was recorded in dependence of the polar angle.

Both LEED and XPD support an epitaxial growth of Ti on Al in form of islands. The structure of the Ti overlayer is pseudomorphic *fcc*. A distortion of the overlayer was measured with LEED. The interlayer distance of the first two Ti overlayer is smaller than that for the bulk Al as can be concluded from a shift of the forward-scattering peak in the diffraction pattern for Ti.

A shift of the forward-scattering peak in the polar angle scan for Al indicates an expansion of the first top layers in the Al substrate. Due to the absence of a strong forward-scattering peak in the Al scan for coverages above three monolayers the interdiffusion of bulk Al into the Ti film can be ruled out.

The Ti overlayer exhibits no long-range order for coverages of eight monolayers but still shows short-range order according to XPD.

CHAPTER 1

Introduction

For the development of state-of-the-art electronic device technology the growth of ultrathin epitaxial films on single-crystal substrates becomes more and more important. The growth of epitaxial films and the formation of metastable phases of the overlayer material lead to new directions in the search for new materials. These phases are occasionally the result of lattice mismatches which lead to a structure that is different from the equilibrium one at room temperature.

For example, face-centered cubic (*fcc*) Co films grow epitaxially on Cu(001) substrates [1], [2]. Both Al and Au can in principle grow epitaxially on GaAs(001) by nucleating an *fcc* overlayer in which the surface unit mesh of the overlayer is rotated by 45^o with respect to that of the substrate [4].

Saleh and coworkers as well as Jona et.al. previously studied the growth of thin Ti films on Al(110) and Al(100) surfaces [6], [21]. Thin Ti films are of considerable interest for their application as diffusion barriers in semiconductors. The main conclusion of the work by Saleh et.al. was that Ti deposition on Al(110) results in the formation of an epitaxial Ti overlayer. A critical thickness of this metastable overlayer is reached for approximately 5 monolayers (ML) as reported by Saleh [6]. Saleh showed that the Ti adopts the surface symmetry and lattice constant of the underlying Al and forms an *fcc* overlayer. This is particularly interesting since the *fcc* structure of Ti does not occur in the equilibrium phase diagram of Ti at any temperature [3]. Saleh further concludes using the VEGAS-simulation of shadowing of the Al atoms by overlaying Ti atoms that the Ti does not form islands.

The situation for coverages exceeding 5 ML is not clear however. Two different growth modes are suggested: Island formation for Ti coverages above 5 ML and interdiffusion of Ti and Al atoms at the interface.

The present study examines the growth of Ti films on Al(110) surfaces using X-ray photoelectron diffraction (XPD) to supplement the results by Saleh. XPD is well suited to the study of the structure of very thin transition-metal films, because XPD diffraction patterns are collected from each chemical species in the sample independently. These patterns arise primarily from the local structure of a few atomic shells surrounding the emitting atom, so that long-range order is not necessary.

Through XPD we hope to gain an even better understanding of the epitaxial growth of Ti on the Al(110) surface. Ti films of up to 9 ML were deposited on the Al single crystal and the atomic structure of both the overlayer and the substrate were studied *in situ*. XPD measurements were done for clean Al and at coverages of 1.8 ML, 2.5 ML, 4.8 ML and 8.9 ML of Ti. A separate set of LEED experiments were carried out at 1.9 ML, 5.5 ML, and 8.1 ML coverages of Ti.

CHAPTER 2

Experimental Setup

A very clean surface free of contaminants is necessary for conducting experiments that involve surface phenomena. The experiments were therefore carried out in an ultrahigh vacuum chamber.

In our study the chamber is connected to a VAN DE GRAAF accelerator allowing the use of RUTHERFORD backscattering to determine the thickness of the deposited layer. Furthermore the chamber is equipped with an X-ray photoelectron spectroscopy system to do X-ray photoelectron diffraction and with reverse view low energy electron diffraction (LEED) optics for LEED analysis.

The present chapter gives an overview of the system and the experimental setup.

The Ultrahigh Vacuum Chamber

All experiments were performed in an ultrahigh vacuum (UHV) chamber. The use of such a vacuum chamber is crucial for the investigation of surface phenomena because it minimizes contamination of the sample. At pressures below 10^{-10} *Torr* (UHV environment) it takes several hours for the sample surface to become contaminated by the adsorption of residual gas atoms. In addition, UHV environments are beneficial for all ion- and electron-based surface analytical techniques, because the mean-free-path of electrons and ions is very short at atmospheric pressure.

Schematic views of the chamber and its components are shown in Figures 1 and 2. The UHV chamber is made of stainless steel and the inside is lined with *mu metal*

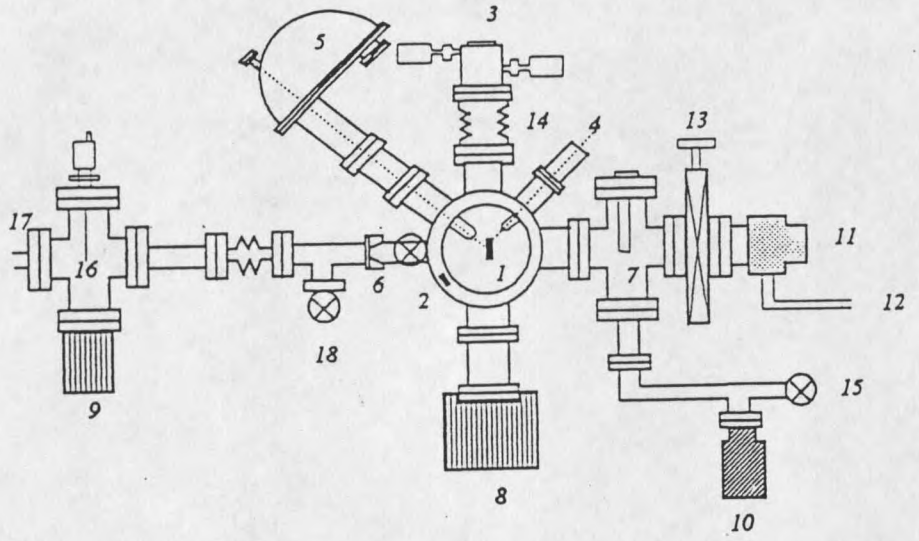

Figure 1: Schematic side view of the chamber

1. Sample	7. Ti sublimation pump	13. Gate Valve
2. Detector	8. Ion Pump	14. Bellows
3. Goniometer	9. Ion Pump	15. Leak Valve
4. Sputter Gun	10. Sorption Pump	16. Beam Blocker
5. Hemispherical Analyzer	11. Turbo Pump	17. Ion Beam Line
6. Collimator Slits	12. Foreline Pump	18. Valves

to provide magnetic shielding.

The chamber is equipped with a turbomolecular pump (*Balzers TPU 160*), an ion getter pump (*Varian*), and a titanium sublimation pump. To reach a regime in which the UHV pumps are operable a roughing pump with a foreline trap is connected to the chamber through the turbomolecular pump. An ionization gage and a quadrupole residual gas analyzer (*Dycor Electronics M100M*) are mounted to the chamber to monitor the pressure as well as the gas composition in the chamber. A pressure in the low 10^{-10} *Torr* range is obtained by baking the chamber at 150^0C for about 48

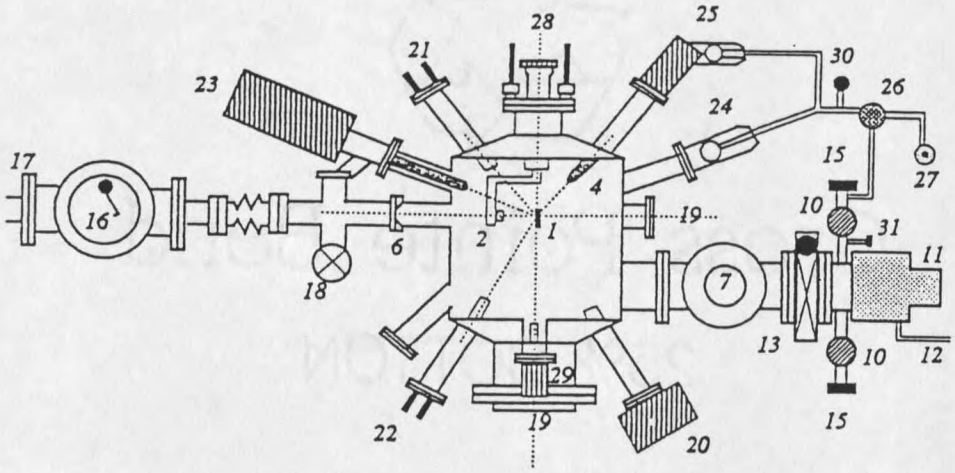

Figure 2: Schematic top view of the chamber

19. LEED Optics
20. Residual Gas Analyzer
21. Ti Filament
22. Ti Filament
23. X-ray Gun
24. Leak Valve
25. Sputter Gun Leak Valve
26. Gas Reservoir
27. $Ar/H_2/O_2$ Gas Bottles
28. Detector Arm
29. Ion Gage
30. Valves
31. Vent Valve

by baking the chamber at 150^0C for about 48 hours.

The Accelerator and Helium High Energy Particle Detector

A VAN DE GRAAF accelerator and a particle detection system are used to align the sample as well as to find the thickness of the deposited overlayer. The accelerator provides a high energy He^+ beam, which is well focused and collimated. It is connected to the chamber via a differentially pumped beam line.

He (or H) ions are generated in a discharge tube by means of an *rf*-field. The ions

are accelerated down a column and then deflected by a bending magnet. Since ions of different kinetic energy will not be deflected through the same angle, only the ions with the desired kinetic energy will be deflected into the scattering chamber.

The beam line contains two apertures 1 mm in diameter. These apertures collimate the beam and also allow for differential pumping of the beam line. The beam line is also equipped with two slit jaws opposite one another. These jaws allow us to monitor the beam current, and, since they are part of a feedback circuit to the accelerator, correct for possible fluctuations in the energy of the particles.

The number of ions incident on the sample is calculated by integrating the sample current over time. The total number of incident ions is then equal to the integrated charge divided by the charge of an ion.

The X-ray Photoelectron Spectrometer

X-ray photoelectron diffraction uses the typical setup for X-ray photoelectron spectroscopy (XPS) while the sample is tilted through a certain polar angle. The X-ray source and the analyzer are kept stationary. The following is a description of the X-ray photoelectron spectrometer used.

The X-ray photoelectron spectrometer shown in Figure 3 consists of the following components: X-ray source, electrostatic analyzer, and counting electronics. The twin anode X-ray source (*VSW TA10*) provides X-rays of Al K_α (1486.6 eV) and Mg K_α (1253.6 eV). The linewidth for the X-rays of Al K_α is 0.85 eV. Only the Al anode was used during the following experiments. Water cooling is necessary to remove excessive heat from the anode. During our experiments a filament current of 2.5 A, an emission current of 25 mA, and an anode voltage of 12.5 kV were used.

A hemispherical analyzer (*VSW HA100*) measures the energy of the photoelectrons emitted from the surface of the substrate. The analyzer is equipped with a

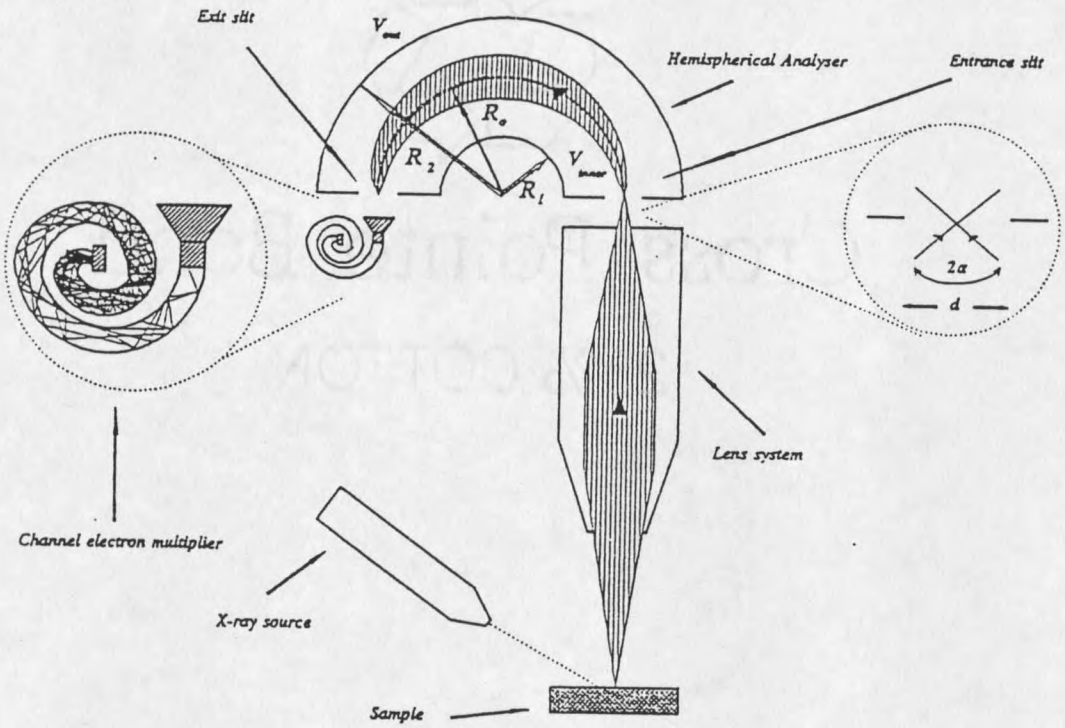

Figure 3: X-ray photoelectron spectroscopy system

control unit (*VSW HAC5000*) which supplies the appropriate voltages for the lenses, hemispheres, and the electron multiplier. Our measurements were carried out in what is called the fixed analyzer transmission (FAT) mode, in which a fixed pass energy for the electrons is maintained. Electrons with various kinetic energies are retarded according to their kinetic energy so that they enter the hemispherical analyzer with a fixed pass energy. In the FAT mode these pass energies together with the retarding ratios can be selected. A pass energy of 50 eV is used, giving reasonable energy resolution of 1.0 eV. A scan rate of 0.1 eV/s is chosen to scan individual peaks.

The emitted photoelectrons enter the hemispherical analyzer and only those photoelectrons with a predetermined kinetic energy are detected by the detector. The detector used here is a single channel electron multiplier (channeltron) for the detec-

tion of energy-selected electrons. The channeltron is a small glass tube. The inside is coated with high-resistance material. Electrons incident on the inside wall cause the emission of secondary electrons, which in turn are accelerated inside the tube and after hitting the wall generate more secondary electrons. This cascade of accelerated electrons produces a large number of electrons at the high voltage end of the tube. In about 10 nanoseconds one electron at the low voltage end can produce 10^8 electrons at the high voltage end. A pre-amplifier is used to further amplify these pulses, which are then transmitted to the multichannel analyzer.

The yield is recorded with a PC-based acquisition system. The scan rate and the total number of counts of the electron pulse determine the total yield. For more information on data acquisition see [7].

For X-ray photoelectron spectroscopy the sample, which is grounded, is tilted through a certain polar angle. In our setup this angle is limited to a range between 3^0 and 53^0 because of the dimensions of the goniometer and the sample holder.

The Reverse View Low Energy Electron Diffraction Optics

All qualitative low energy electron diffraction (LEED) measurements are performed in the vacuum chamber which is equipped with a reverse view LEED optics (RVL 6 - 120, Princeton Research Instruments). A schematic diagram of the LEED optics is shown in Figure 4.

As can be seen from Figure 4 the instrument consists of four nested hemispherical grids (G1 - G4) and a hemispherical glass collector screen (C). The collector screen is coated with an optically transparent film of tin oxide over which a uniform layer of phosphorescent material is applied. This coating is excited by incoming electrons and emits visible light. The electron gun is mounted through a hole in the middle of the grids and the screen. Grids 2 and 3 are known as the suppressor grids.

The electron gun on the left of Figure 4 provides a focused electron beam at the surface of the sample. Currents of 25 to 50 μA may be produced. F1 and F2 are the feedthroughs of the thoriated iridium filament, which is extremely resistant to burnout. An extraction voltage (V1) controls the beam emission. The two other optical elements, which are connected through V2 and V3, provide focus and collimation of the beam.

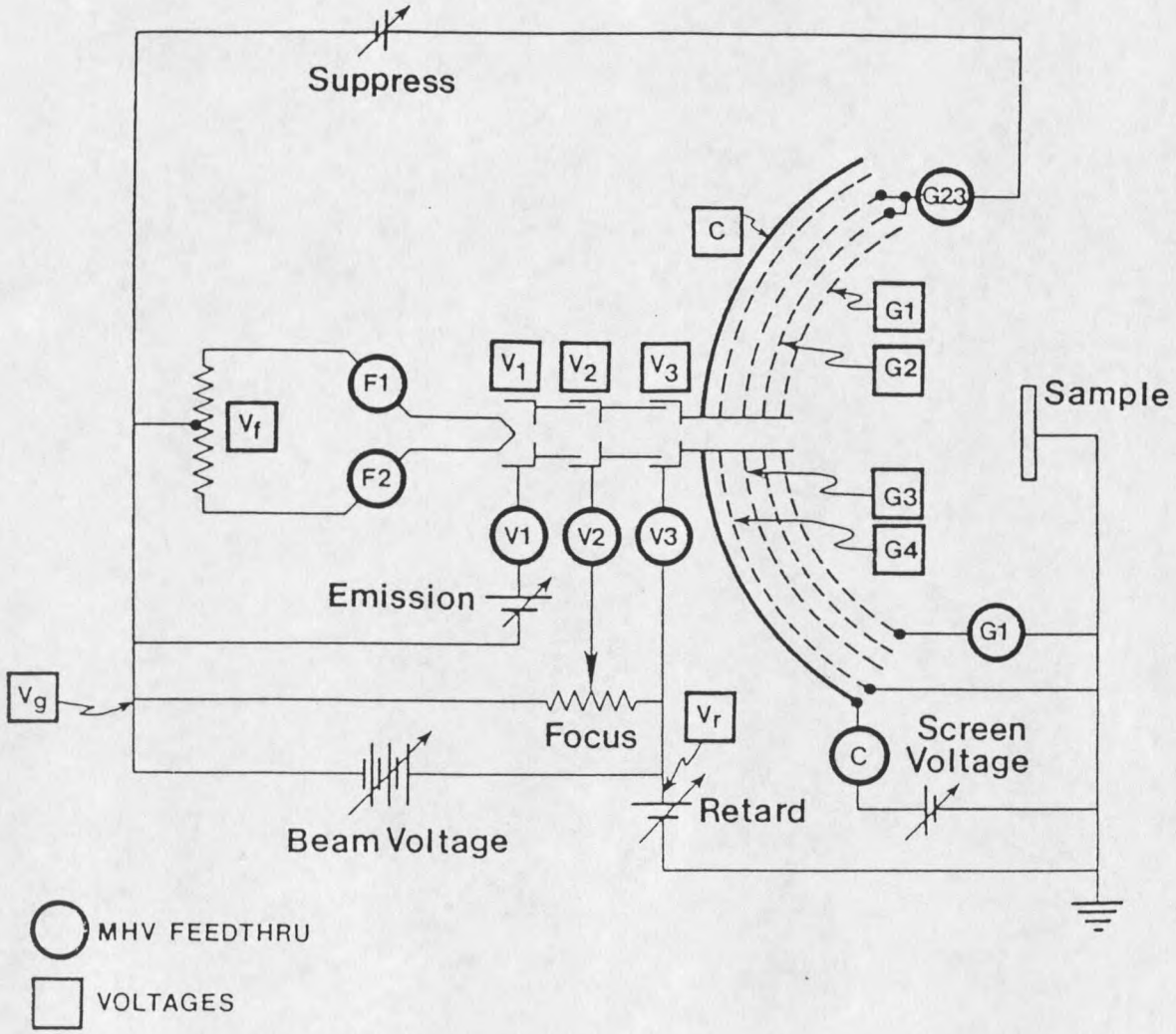

Figure 4: Schematic diagram of the LEED optics and electrical connections

CHAPTER 3

Experimental Techniques

X-ray photoelectron diffraction (XPD) is the main analytical technique used in this thesis to receive information about the surface structure in this study. Low energy electron diffraction (LEED) is used to complement XPD and to gain additional information about the long range order of the surface. High energy ion scattering (HEIS) or RUTHERFORD backscattering (RBS) is used to align the sample and determine the thickness of the overlayer.

In this chapter the basic physical principles of the various surface analytical techniques used including sample preparation will be introduced.

Sample Preparation

A well ordered surface is necessary for an epitaxial film to form on any surface. That is why the Al(110) crystal is thoroughly prepared before it is put into the vacuum chamber. This preparation includes polishing, as well as sputtering and annealing after the sample is put back into the chamber.

To obtain a smooth and shiny surface the crystal is polished on silicon carbide paper (grit size 400) and *Buehler alpha micropolish* alumina particles of decreasing particle size ($5\mu m, 1\mu m, 0.3\mu m, 0.05\mu m$). For the polishing procedure the crystal is mounted in a polisher-goniometer to ensure proper surface alignment. The orientation is checked using LAUE X-ray diffraction. Finally the crystal is polished with a SYTON solution. After each step the crystal is cleaned with acetone, methanol, and deionized water.

Polishing damages the top layers of the crystal. To remove these layers the crystal is chemically etched in a solution that contains 95 % deionized water, 1.5 % hydrofluoric acid (HF), and 2.5 % nitric acid (HNO_3).

The dry sample is then mounted onto the goniometer via a sample holder. The goniometer allows us to rotate the sample independently about three orthogonal axes as well as to translate the sample up and down. After evacuating the chamber the sample is sputtered in vacuum with Ar^+ ions to remove the thick Al_2O_3 oxide layer as well as other possible contaminants from the surface. Argon gas is slowly leaked into the ionization chamber of a 5kV sputter gun, where the Ar molecules are excited by impact of electrons. The Ar^+ ions are then accelerated and focused onto the sample surface. The sample is sputtered for about three hours. The process is monitored by XPS.

Figure 5 shows the XPS spectrum of the Al 2p core level before and after sputtering. The spectrum of the contaminated substrate displays a definite oxide peak to the left of the Al peak. The Al_2O_3 peak is clearly missing from the spectrum of the clean surface. After sputtering the sample is annealed for about 15 minutes at a temperature of 520^oC. The elevated temperature removes possible damage from the sputter beam and allows impurities such as oxygen from the bulk to diffuse to the surface where it is sputtered off subsequently. This cycle of annealing and sputtering is repeated until the oxide peak has vanished. The surface is then assumed to be clean.

After it is decided that the sample is clean a thin Ti film can be deposited onto the sample surface. This is done using a wire evaporation source. It consists of twisted strands of Ti wire (99.99 % purity) 0.25 mm thick and about 8 cm in length that are wound into a coil. Before these strands are spotwelded to the feedthroughs they were etched in a 20 % HF solution. A constant current is applied to these filaments

to obtain a constant Ti sublimation rate. The filaments are mounted about 13 cm away from the sample. The correct deposition rate for each of the filaments (time of deposition for constant current) was determined through several trial runs. RUTHERFORD backscattering was used to measure the exact total Ti coverage throughout the experiment.

High Energy Ion Scattering

High energy ion scattering (HEIS) or RUTHERFORD backscattering (RBS) is used to determine the thickness of the deposited Ti overlayers. Measuring the layer thickness using RBS is highly accurate and avoids estimations of the overlayer coverage that may lead to errors of up to 100 % [21]. The accuracy of the thickness measurement is directly determined by the accuracy of the measured beam-detector characteristics.

Figure 6 shows an RBS spectrum for about 9 monolayers (ML) of Ti on an Al substrate. It shows the edge of the Al substrate and the peak due to the Ti overlayer to the right. Two numbers can be identified from such a spectrum: the energy width ΔE between the two edges of the signal for the film, and the total number of counts contained in all channels between these edges. Both quantities are directly related to the thickness of the film.

While we use the total number of counts added over all channels in the film signal to determine the number of atoms per unit area and ultimately the thickness of the film, it is first necessary to determine the exact energy of the incident ions. A collimated and focused He^+ ion beam is incident on the substrate with a kinetic energy of about $E_i = 0.96\ MeV$ and an ion current of about 30 nA. Ions with energies around 2 MeV are energetic enough to penetrate deep into the substrate and interact with the nuclei of the substrate atoms. The energy loss due to scattering

can be calculated using momentum and kinetic energy conservation and leads to the following equation:

$$E_1 = \frac{1}{(1+\frac{m_2}{m_1})^2}\left[cos\theta + \left(\left(\frac{m_2}{m_1}\right)^2 - sin^2\theta\right)^{\frac{1}{2}}\right]^2 \cdot E_0 \qquad (1)$$

This equation can be abbreviated by introducing K the kinematic factor:

$$E_1 = KE_0 \qquad (2)$$

where K is a function of θ and $\frac{m_2}{m_1}$. Here m_1 and m_2 are the masses of the incident and target particle, θ the scattering angle, and E_0 the kinetic energy of the incident particle and E_1 the energy of the scattered particle. Equation (1) also shows the possibility of element identification for the target particle m_2. For further discussion of the limits of this approach see [5].

Particles scattered from an atom at rest cannot have energies above KE_0. KE_0 therefore represents an edge in the backscattering spectrum corresponding to scattering from surface atoms. The kinematic factor K for the substrate Al and the energy of the edge in the Al RBS spectrum E_1 yield the incident energy of the He^+ ions E_0.

Introducing E_2 as the energy of a particle scattered from an atom at a certain depth leads to the energy width ΔE:

$$\Delta E = E_1 - E_2 = KE_0 - E_2 \quad . \qquad (3)$$

The incident energy E_0 of the ions is necessary to calculate the layer thickness via the total number of counts or the total backscattered ion yield Y. A brief summary of the theory behind the thickness determination follows.

For normal incidence, the total number of detected particles Y can be written as

$$Y = \frac{d\sigma}{d\Omega} \cdot d\Omega \cdot Q \cdot Nt \quad , \qquad (4)$$

where Q is the total number of incident particles that hit the target and $\frac{d\sigma}{d\Omega}$ the differential scattering cross section. If N is the volume density and t the thickness of the layer, then Nt is the number of target atoms per unit area or areal density. For known volume density and differential cross section for the element, the thickness can be calculated as

$$t = \left[\frac{Y}{d\Omega \cdot Q \cdot N} \cdot \frac{1}{\frac{d\sigma}{d\Omega}} \right] \quad . \tag{5}$$

The total number of incident particles Q is determined from the integrated charge, and the total yield Y is calculated from the spectrum. This equation uses a constant differential cross section. Since $\frac{d\sigma}{d\Omega}$ is depended on the incident energy the equation is valid only in the surface energy approximation, e.g. if $E \simeq E_0$. This is the simple case of a film thin enough that the energy loss of an incident particle is negligible compared to its initial energy E_0. In this case the scattering cross section is constant throughout the whole film.

A computer program based on this equation calculates the layer thickness using the type of scatterer atoms, the incident energy, the integrated charge, the number of atoms per row for Al(110), and the scattering angle as input parameters.

X-Ray Photoelectron Diffraction

X-Ray Photoelectron Spectroscopy

X-ray photoelectron diffraction (XPD) is based on the technique of X-ray photoemission spectroscopy (XPS or ESCA). It is a particular mode of detecting photoelectrons in a photoemission experiment that allows one to obtain structural information which is not possible for regular X-ray photoemission spectroscopy .

XPS uses the interaction of incident photons, with energies above 100 eV and target atoms. The underlying effect is the so called photoelectric effect. Photons

are generated using an X-ray source, which consists of a hot wire Al filament, an Al anode and a HV supply. Ionization of the Al atoms in the anode leads to holes in the inner shell, which subsequently are filled through electron transitions, and X-rays are emitted. The energy of the emitted photon is characteristic for each transition, e.g. for an Al anode and a $2p \rightarrow 1s$ transition, K_α X-rays with characteristic energies of 1486.6 eV are emitted. This transition is called the *Al* K_α transition.

The ionization energy I_i of the target atom and the photon energy ($h\nu$) determine the kinetic energy of the emitted electron:

$$h\nu - I_i = E_{kin} \quad . \tag{6}$$

This is called KOOPMANN's Theorem. The positive ionization energy I_i is here equal to the binding energy E_B of the electron relative to the vacuum level. The binding energy can be measured with respect to the vacuum level as well as with respect to the FERMI level . The latter is more common for metals. If we take the difference between the vacuum and the fermi level to be the work function of the sample surface ϕ_s, then the kinetic energy is given by:

$$E_{kin} = h\nu - E_B - \phi_s \tag{7}$$

Because of the specific core-level binding energies for different elements, XPS is element specific and can be used to identify these elements. The maximum kinetic energy for emitted electrons for Al is therefore 1410 eV ($E_B = 78eV, \phi_s = 8eV$). The escape depth for such electrons can be determined using the mean free path of the electrons in the metal, which in turn is based on the general formulation for the energy loss. The mean free path for electrons can be written as

$$\lambda = \frac{hv^2}{\omega_p e^2} \cdot \left[ln \frac{2mv^2}{hv^2} \right]^{-1} \tag{8}$$

where ω_p is the plasmon frequency, with $\omega_p = 4\pi e^2 n/m = 2.27 \cdot 10^{16} rad/s$. We calculate the value for λ to be 16.9 Å for 1410 eV electrons in Al, which corresponds to about 6 monolayers. This value corresponds to the one found from the universal curve [11].

The Ti 2p core-level is split due to spin-orbit splitting as can be seen from Figure 7. The intensities of the characteristic photoelectron peaks are used to monitor the morphology of the overlayers deposited on a solid surface. In order to calculate the peak areas a background underneath the peak has to be subtracted. The background subtraction technique used here is discussed in chapter 4. The background on which the photopeak is superimposed is due to secondary electrons that have undergone inelastic scattering and energy loss. Because of the energy loss these electrons do not contribute to the characteristic photoelectron peak.

Experimental Design

X-ray photoelectron diffraction (XPD) is a technique that is based on the element specificity and surface sensitivity of XPS to investigate and determine the structure of epitaxial overlayers. Due to the element specificity contributions from the substrate can be eliminated, and substrate and overlayer can be distinguished. Since the diffraction patterns are primarily due to the local structure of a few atomic shells surrounding the emitting atom, long-range order is not necessary.

In our application of XPD we use primarily the enhancement of the XPS signal in the forward direction, called *forward focusing*. The sample is rotated to use this angular dependence of the photoelectron intensity while the energy analyzer and the X-ray source are held stationary. Figure 8 shows the geometry of our XPD experiments. Al K_α X-rays are incident on the substrate. The polar angle θ is swept, and different azimuths ϕ are achieved by rotating the substrate about the surface normal.

The forward-focusing effect is also observed for AUGER Electron Spectroscopy. X-ray photoelectrons emitted with kinetic energies of several hundred electronvolts by near surface atoms are scattered by overlaying lattice atoms. This scattering produces enhanced intensities in the directions connecting the atom with its nearest and next-nearest neighbor atoms. Adding the element specificity constitutes a probe of short-range order around a particular element.

Single Scattering Theory

The underlying process for XPD is the elastic scattering of a photoelectron wave portion by atoms in the vicinity of the emitter. A simplified, semiclassical picture of this process is given in Figure 9. A primary X-ray ionizes an atom, resulting in an expanding spherical wave centered on the emitting atom. This outgoing wave Ψ_0 can be represented as

$$\Psi_0(r,\alpha) \propto \sqrt{\frac{d\sigma(\epsilon,k)}{d\Omega}}\frac{exp(ikr)}{r}, \tag{9}$$

where $[d\sigma(\epsilon,k)/d\Omega]$ is the differential cross-section for the ionization event and ϵ the electric field polarization vector for the primary X-ray. The scattered wave portion Ψ_j is spherical as well, and is centered at the scattering site. It is dependent not only on the initial wave amplitude Ψ_0, but also on the so called scattering factor $|f(\theta_j)|$, where j specifies the scattering atom.

$$\Psi_j \propto \Psi_0\frac{exp(ik(|r-r_j|)}{|r-r_j|}|f(\theta_j)|, \tag{10}$$

The scattering factor $|f(\theta_j)|$ is strongly peaked in the forward direction due to the COULOMB interaction between the photoelectron and the ion core. Using classical trajectories to simulate the scattering event it can be said that the closer an electron comes to the ion core, the larger the angle through which it is scattered. In addition

the higher the kinetic energy of that electron, the closer it must come to the core in order to scatter through a given angle. In fact the semiclassical model is highly accurate for higher energies above several hundred electronvolts [8].

The peaking in the forward direction of the scattering factor, also called *forward focusing*, leads to large intensity enhancements along low-index direction [9]. The intensity is given by:

$$I(k,\theta) = |\Psi_j + \Psi_0|^2. \tag{11}$$

This effect is illustrated in Figure 10 for an electron incident on a Cu atom at different energies [8]. The scattering strength falls off rapidly with increasing scattering angle at high kinetic energies.

A scan over different angles with respect to the sample surface leads to peaks at certain angles if the sample structure is ordered. The angle at which the forward-scattering peak appears can be used to identify the emitter-scatterer axis, or bond direction. The identification of this axis then allows the characterization of epitaxial structures. Intensity enhancements are observed as soon as a chain of two or more atoms forms in a growing epitaxial film. Two to three monolayers are therefore enough for XPD to identify morphology in epitaxial films.

Not only does the position of the forward-scattering peak identify a low-index direction, but changes in the position of that peak relative to what is expected for the bulk crystal are a measure of changes in the interplanar spacing normal to the surface as indicated in Figure 11. Such changes are expected if there is a lattice mismatch between the substrate and the epitaxial film.

One consequence of multiple forward scattering is the so called defocusing effect. It describes the way in which multiple forward scattering disperses a forward-scattering peak. A trajectory that is scattered into the forward direction by the first scat-

terer may be scattered away from that direction by consecutive scattering events. Figure 12 represents the essence of the defocusing mechanism. As the number of scattering atoms above the emitter increases, forward scattering is not as likely to occur since the initial conditions for a trajectory that results in forward-scattering become more and more restrictive. Trajectories are bent away from the forward-scattering direction. The intensity of the peak diminishes. Four atoms following an emitter can completely destroy the forward-scattering enhancement expected in a single-scattering theory [15].

Secondary electrons emitted from crystal surfaces also show strong enhancement along directions defined by atomic rows [16]. The results of imaging such electrons can be interpreted in terms of KIKUCHI patterns [17]. This is mentioned here to motivate the normalization of the polar angle scans in a later chapter.

Low Energy Electron Diffraction

A reverse view LEED optics is used to provide information about the long range order and the orientation of the crystal lattice. LEED uses the diffraction of low energy electrons to determine the structure of the first few layers of atoms of any given crystal.

For electrons of an energy of 20 to 500 eV, the DE BROGLIE wavelength $\lambda = h/mv$ is between 0.05 to 0.3 nm, and therefore in the range of atomic distances. Electrons of that energy directed toward the crystal are diffracted by the surface atoms. The diffracted electrons become visible when they excite the phosphorescent material of a spherical screen. These LEED patterns show the symmetry of the surface without distortions as long as the incident electron beam is normal to the sample surface.

The relation between the diffraction pattern and the *k space* for electrons incident perpendicular to the surface is shown in Figure 13. A flat screen would show a pattern

that is proportional to the projection of the *Ewald sphere* along the k vectors. It therefore shows the cross sections through the k vectors of the reciprocal space. The distortions due to the bending of the *Ewald sphere* are canceled out by a spherical screen.

Increasing the incident energy of the electrons decreases their wavelength and therefore increases the radius of the *Ewald sphere*. The angles between diffracted beams become smaller and the spots on the screen move closer together.

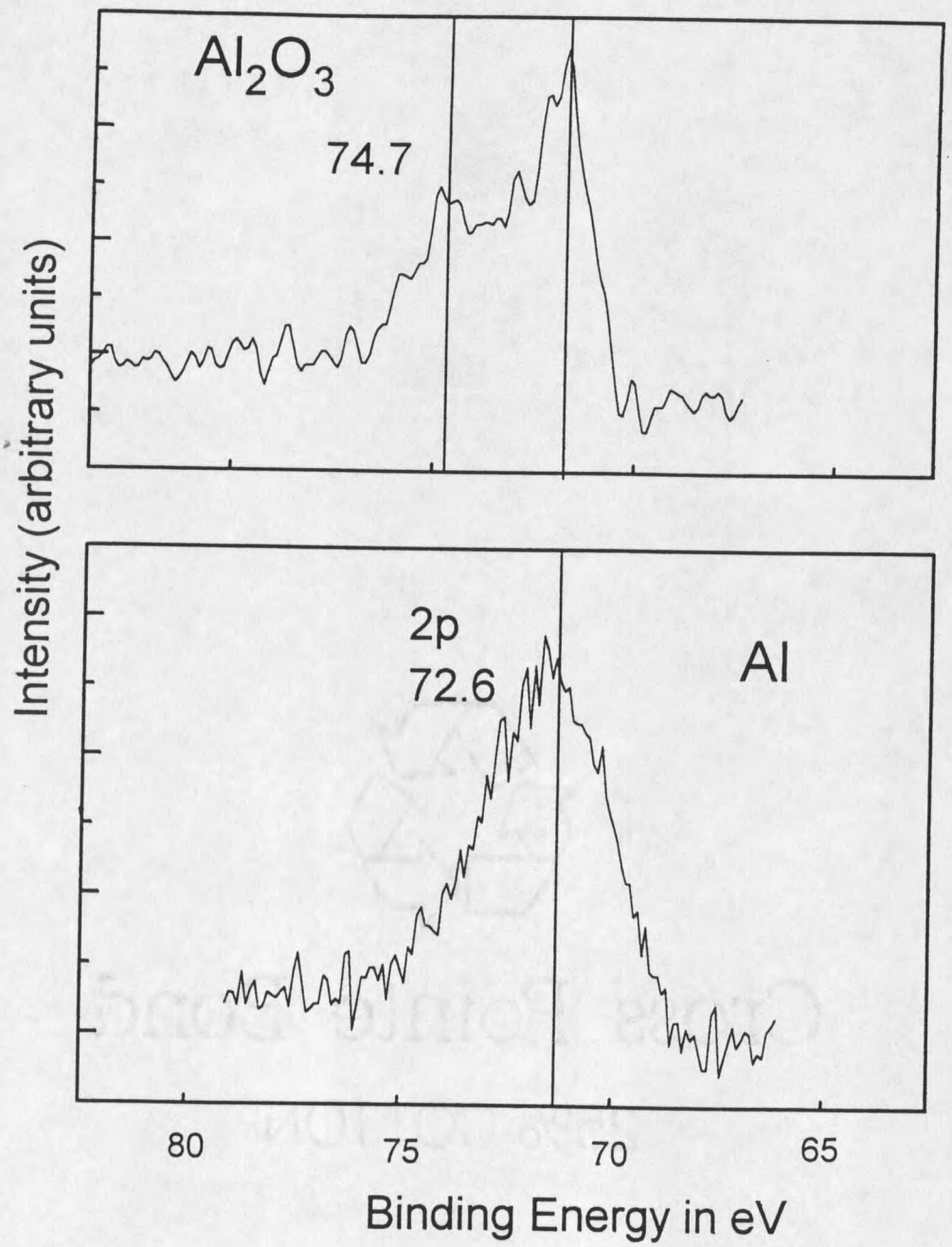

Figure 5: XPS spectrum of the Al 2p peak for (a) before sputtering and (b) after sputtering showing the clean crystal.

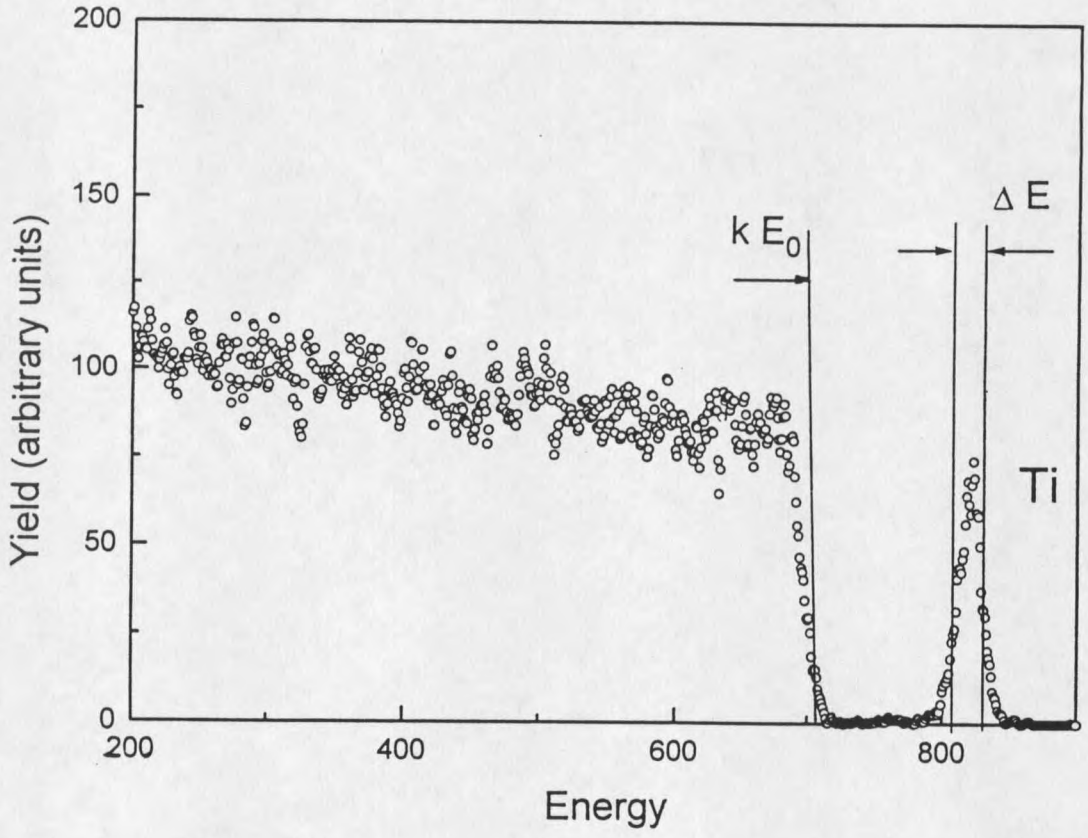

Figure 6: RBS spectrum for an 8.9 ML thick Ti overlayer on Al

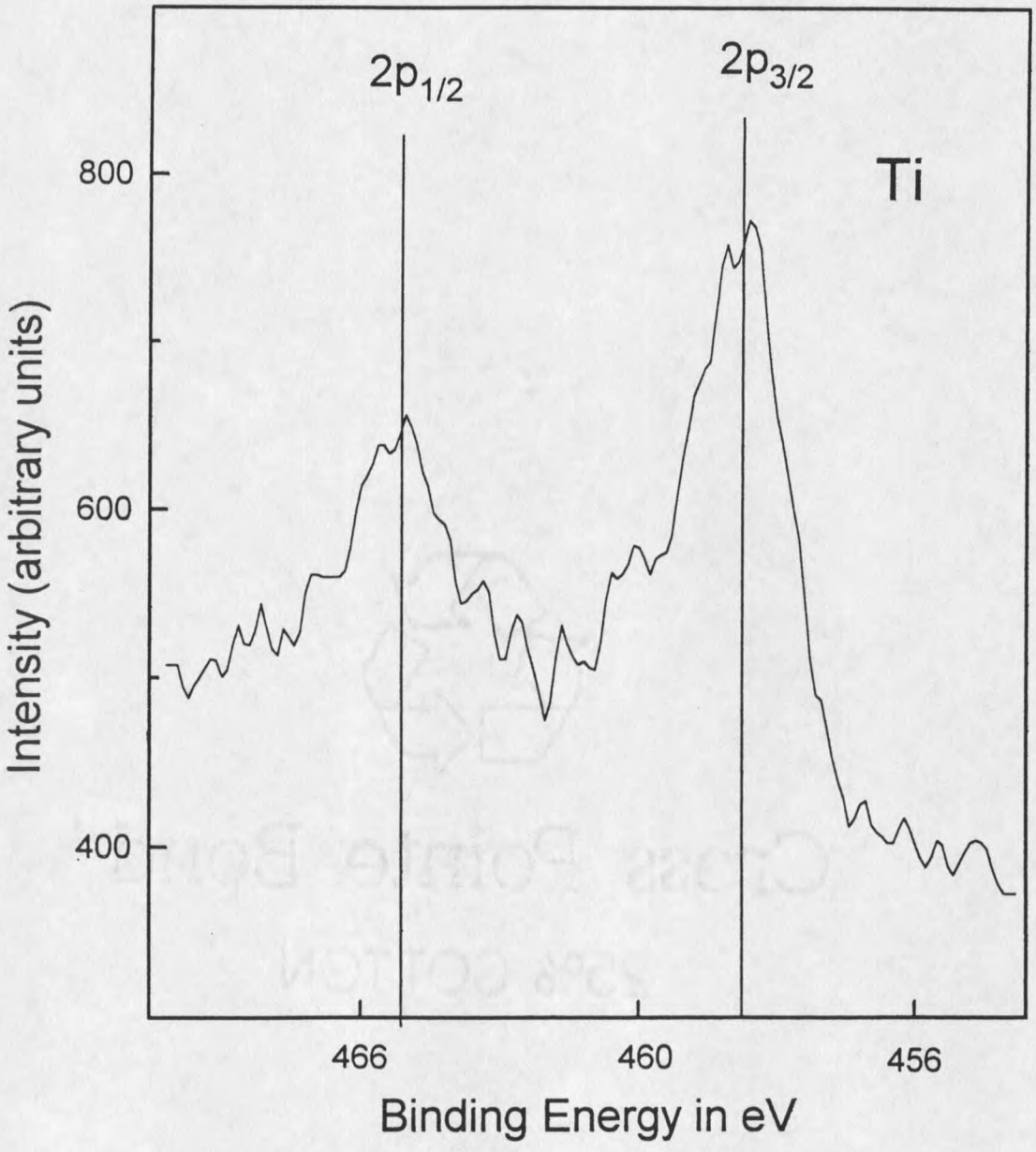

Figure 7: XPS spectrum of Ti. The Ti 2p core-level peak is split due spin-orbit interaction.

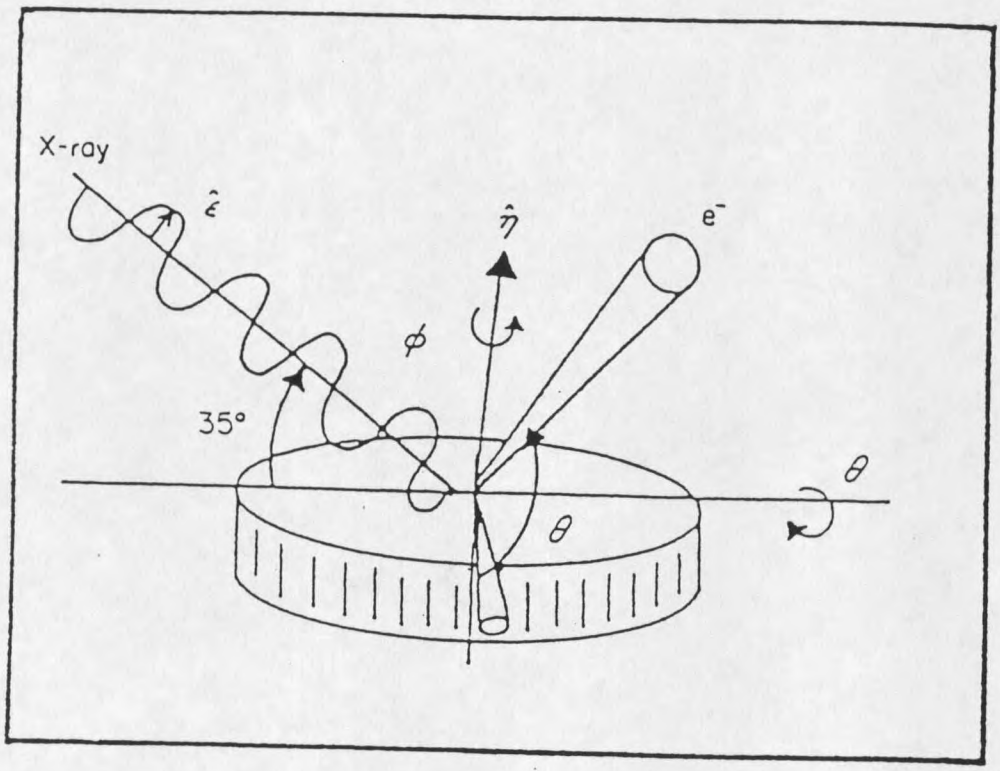

Figure 8: Geometry of the XPD experiment

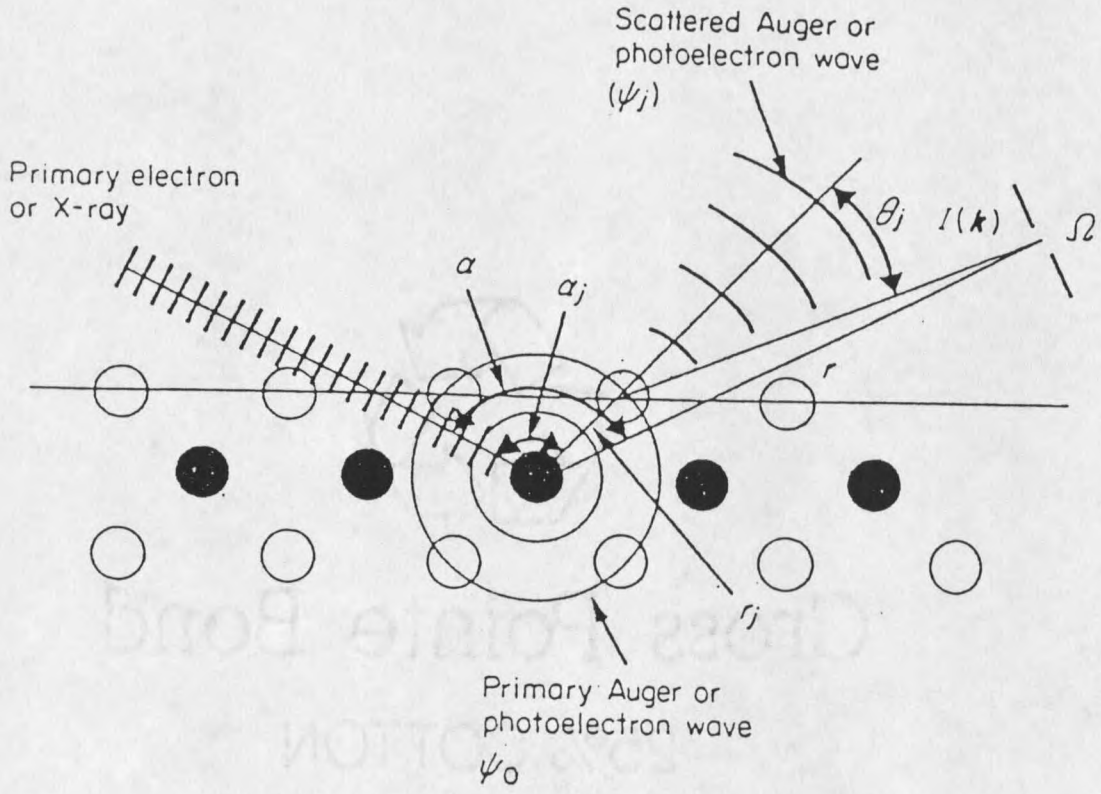

Figure 9: Schematic representation of the XPD experiment

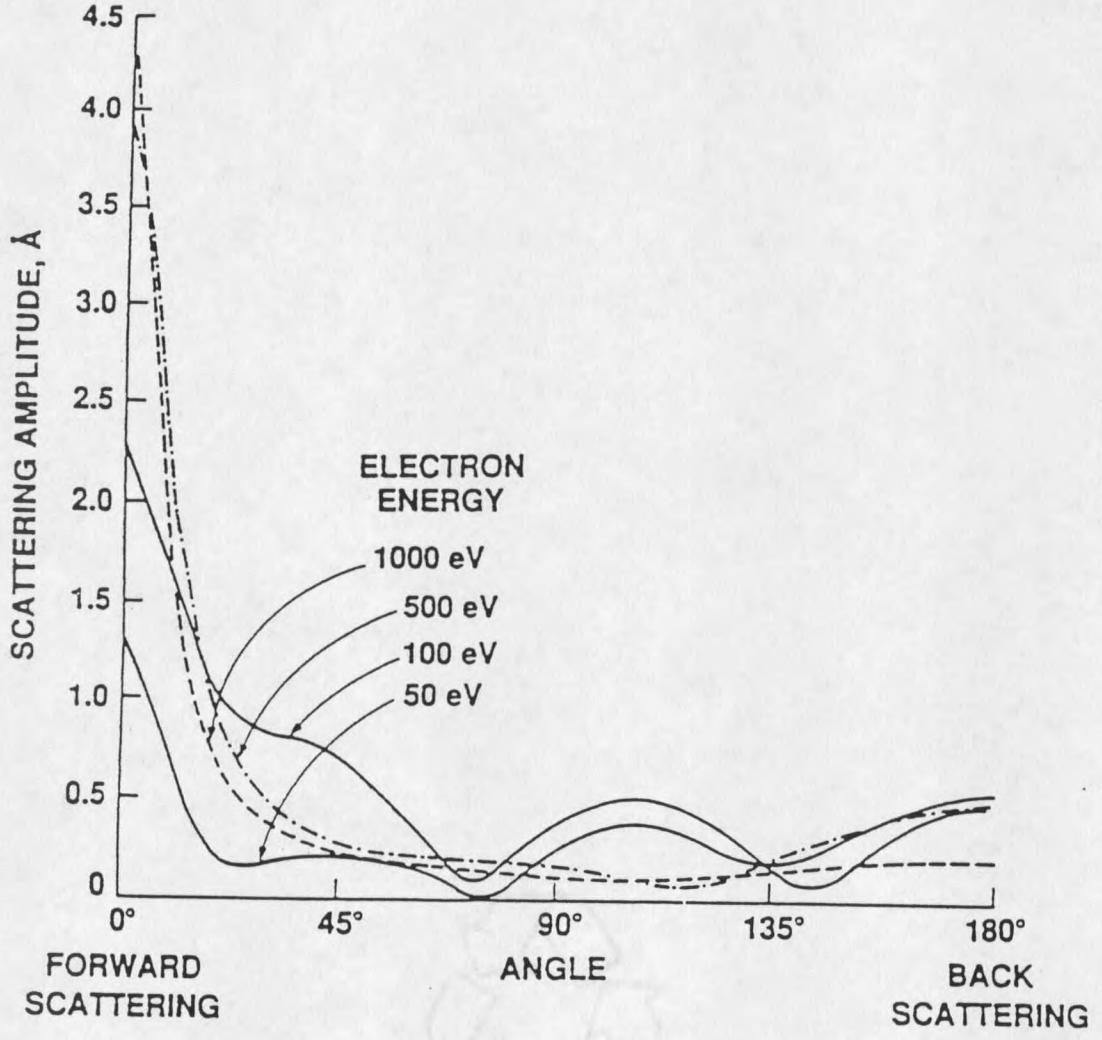

Figure 10: Scattering amplitude for an electron plane wave incident on a Cu atom at different energies [9]

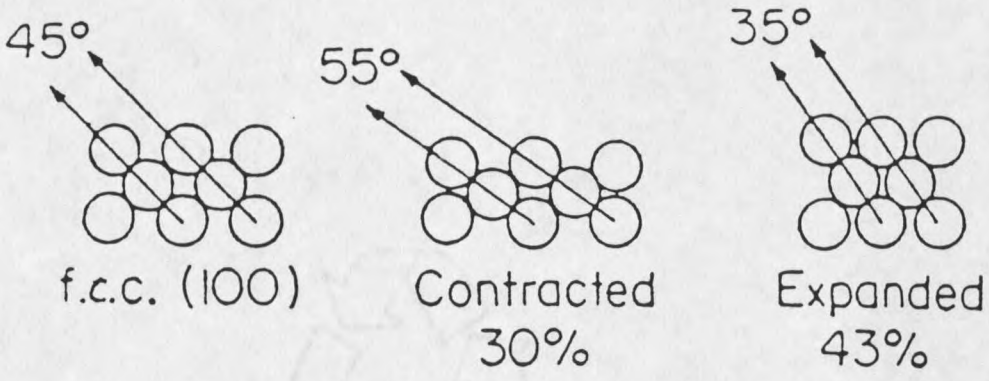

Figure 11: Structural diagram illustrating the interplanar distortion that can be achieved by pseudomorhic growth.

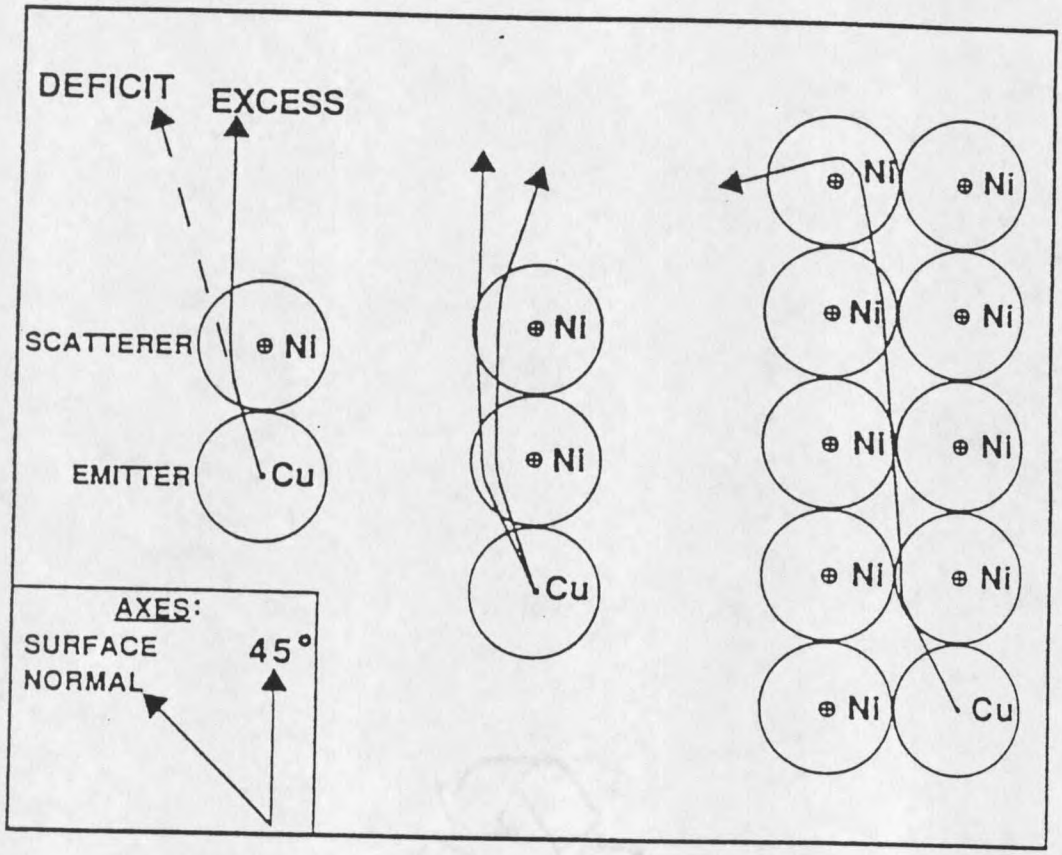

Figure 12: Defocusing effect. The first one or two scattering events tend to be forward-focussing and subsequent events tend to be defocusing.

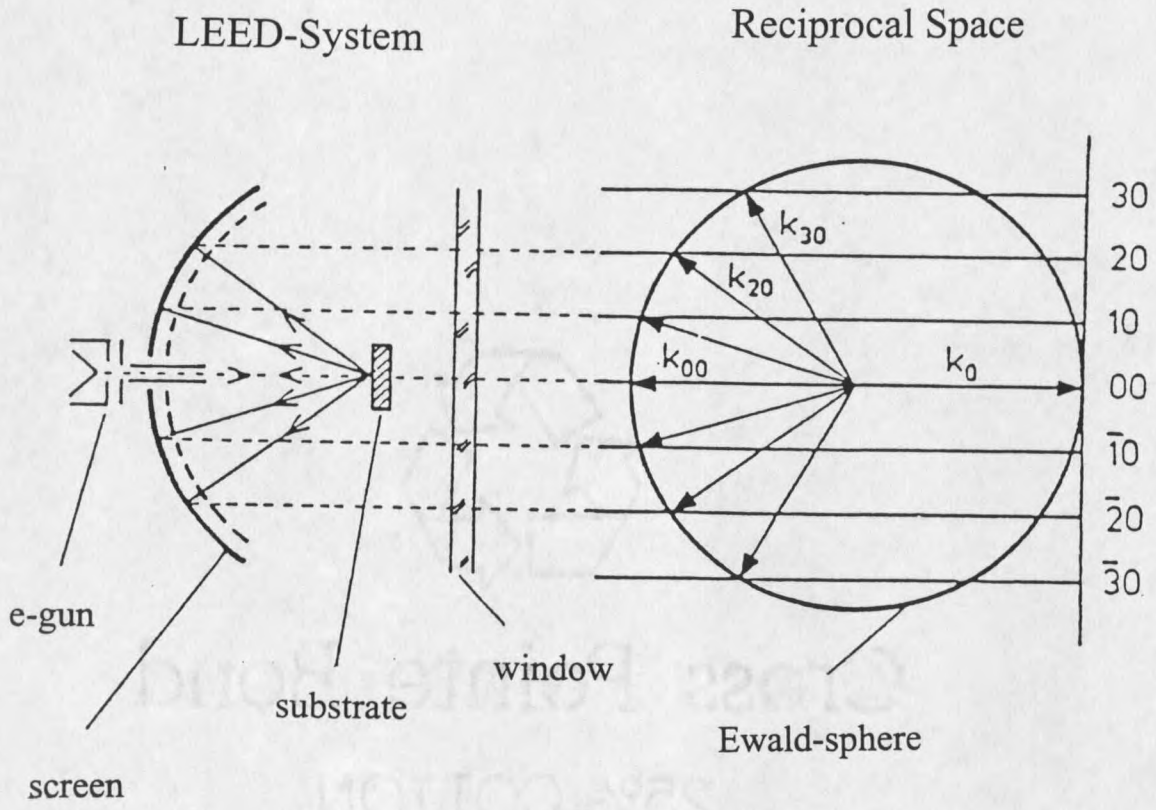

Figure 13: Relation between the LEED diffraction pattern and the reciprocal *k space*

CHAPTER 4

Experimental Results for the Deposition of Ultrathin Ti Films on Al(110)

Rutherford Backscattering

RUTHERFORD Backscattering is used to determine the thickness of the Ti overlayer. A typical RBS spectrum is shown in Figure 6. Due to its higher mass the peak for the Ti overlayer shows up to the right of the backscattered ion energy for the Al substrate.

Table 4.1 shows the different deposition parameters and the resulting thicknesses for two sets of experiments. The layer thicknesses are calculated as described in chapter 3 using $0.8622 \cdot 10^{15}$ *atoms/monolayer* for Ti to convert from an areal density to the thickness.

X-Ray Photoelectron Diffraction

Curve Fitting

The following paragraphs describe the curve fitting and proper background subtraction procedures for the XPS peaks and show how the XPD data are presented.

XPD uses the area under the $2p$ Al and the $2p_{\frac{1}{2}}$ and $2p_{\frac{3}{2}}$ Ti peaks for an angle dependent analysis. The experimentally measured curve is fitted with one or two GAUSSIAN line shapes for the Al and Ti peaks respectively. Fitting the peaks with a convolution of the actual line shape (LORENTZIAN) and the instrument response

Table 1: Deposition Parameters and resulting thicknesses

Deposition Time (min)	Current (A)	Peak Area (counts)	Integrated Charge (μC)	Layer Thickness
XPD Measurements				
6	4.5	279	1.5	1.81 ML
9	4.5	416	1.5	2.5 ML
16	4.5	789	1.5	4.8 ML
19	4.5	1463	1.5	8.9 ML
LEED Measurements				
4	4.5	630	3	1.9 ML
11	4.5	1801	3	5.5 ML
15	4.5	2664	3	8.1 ML

function (GAUSSIAN) for the analyzer and the X-ray source was suppressed as discussed in [5]. The background, which is due to secondary electrons, is expressed in terms of an error function and was subtracted from the measured line using a macro in the program GENPLOT. This method is referred to as SHIRLEY background subtraction [18]. The background is proportional to the integrated photoelectron intensity. Figure 14 shows an Al and a Ti XPS peak. Indicated are the background as well as the peak area after background subtraction.

An angular profile is created by recording the peak area in dependence of the polar angle over an interval of $0 - 50^0$ in 1 degree steps. The actual data sets start at around 3^0 because our experimental setup limited the motion of the goniometer and the sample holder.

In order to be able to compare different data sets with one another, the data sets were normalized. Since secondary electrons emitted from crystal surfaces show forward focusing as well, it is not recommended to simply divide the peak area by the recorded background. Instead, the background was recorded as a function of the angle and then spline fitted. The curve that shows the peak area dependence on

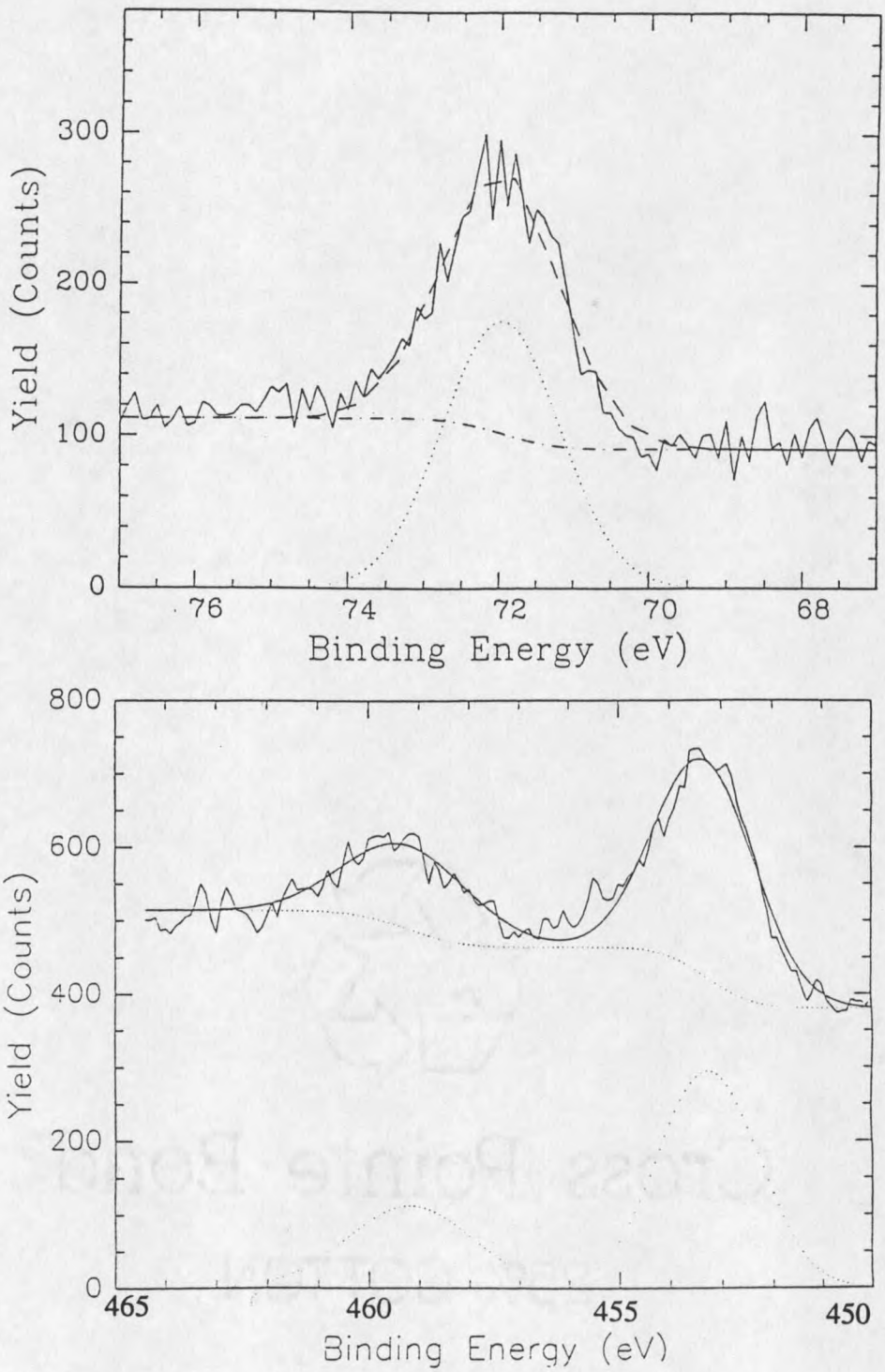

Figure 14: XPS peaks for Al ($2p$) and Ti ($2p_{\frac{1}{2}}$ and $2p_{\frac{3}{2}}$). The dotted line represents the background. The peak areas after background subtraction are shown below the actual peaks.

the polar angle is then divided by this spline fit. Figure 15 shows the polar angle dependence of the secondary electrons and the spline fit through the spectrum of data. The intensity falls off for larger angles because the sample is tilted away from the analyzer.

Results

X-ray photoelectron diffraction patterns were taken in two different azimuths. Figure 16 shows the two crystal directions with the respective angles. The sample was tilted through angles from about 3^0 to 50^0 with respect to the analyzer for the [110] and the [100] substrate azimuths. Since it was not possible to tilt the sample to reach normal incidence, the 45^0 forward-scattering peak for the clean Al surface was therefore used as a reference.

For each azimuth the Al $2p$ and the Ti $2p_{\frac{1}{2}}$ and $2p_{\frac{3}{2}}$ peaks were scanned and the peak areas were recorded as mentioned above. Figure 17 and Figure 18 show the polar angle scans for the Al (110) crystal for both azimuths. The solid line was added to guide the eye. Figures 19 and 20 show the polar angle scans for the Ti signal for both azimuths.

The spectra for the [110] azimuth show more structure than those for the [100] azimuth for both the Al and the Ti photopeaks. The curve for clean Al shows a distinct peak at 45^0 and another around 26^0. The 45^0 peak is due to forward-scattering in this direction which characterizes the *fcc* lattice structure of Al. For a coverage of 1.8 ML of Ti on Al both peaks are shifted toward smaller angles. The spectra for higher coverages in Figure 17 show no definite structure except for the forward-scattering peak at normal incidence (around 3^0). These spectra are only taken for angles up to 37^0, because the signal strength weakens considerably for larger angles.

The spectra taken in the [100] azimuth shown in Figure 18 show no structure except for the peak toward 0^0.

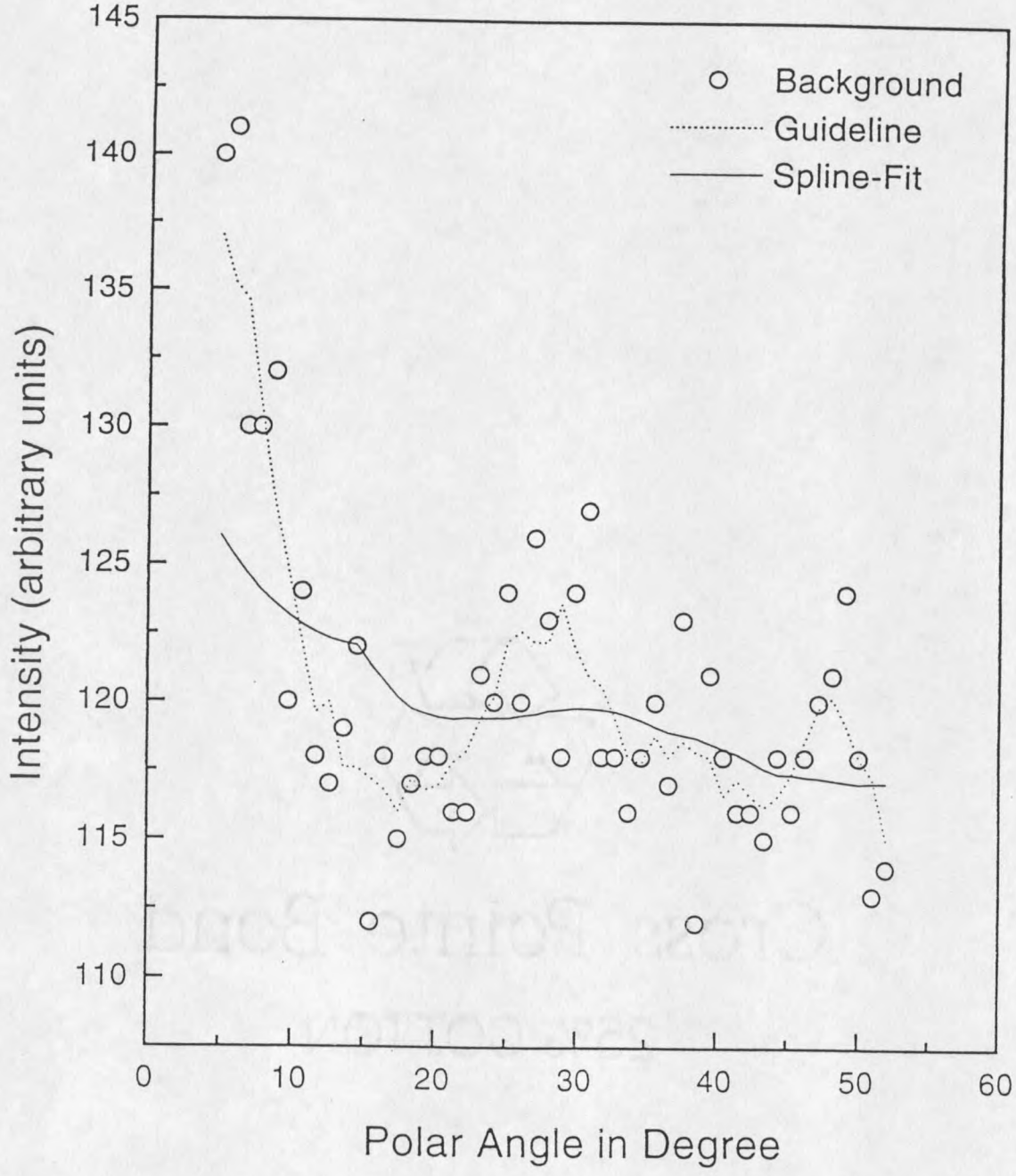

Figure 15: XPD pattern for Al(110) secondary electrons. The figure shows the polar angle dependence of the background and the spline fit through the background.

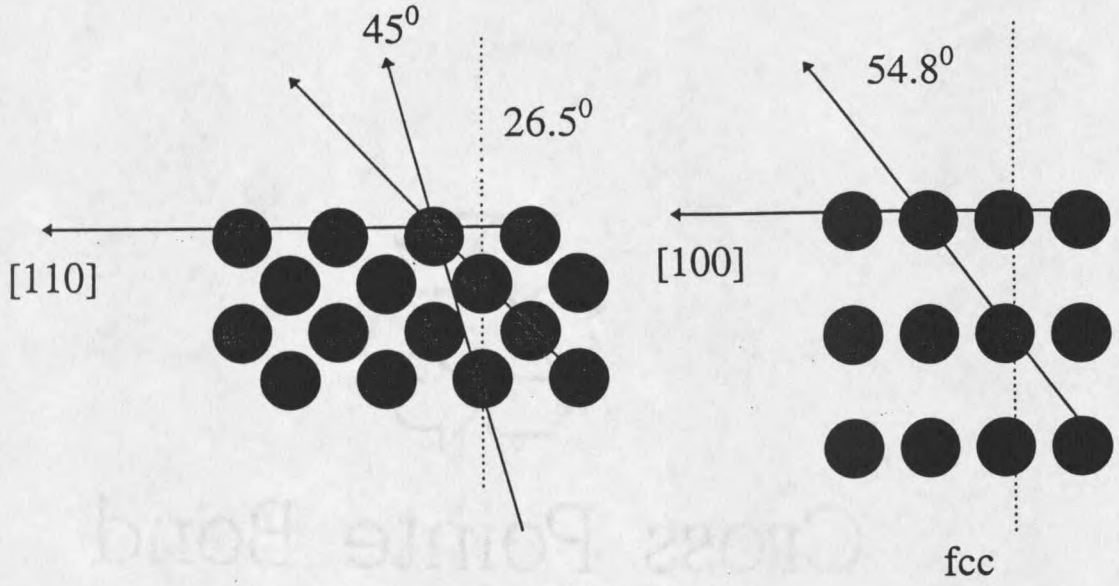

Figure 16: *fcc* crystal direction and respective angles for the [110] and [100] azimuths

The polar angle scans for Ti in the [110] azimuth of Figure 19 show interesting structure and structural changes for higher coverages. There is a small but distinct peak around 45^0. This peak is very pronounced for a coverage of 8.9 ML of Ti.

The [100] azimuth for Ti shows very little structure as was observed for Al in the same azimuth. Only the peak for normal incidence is visible.

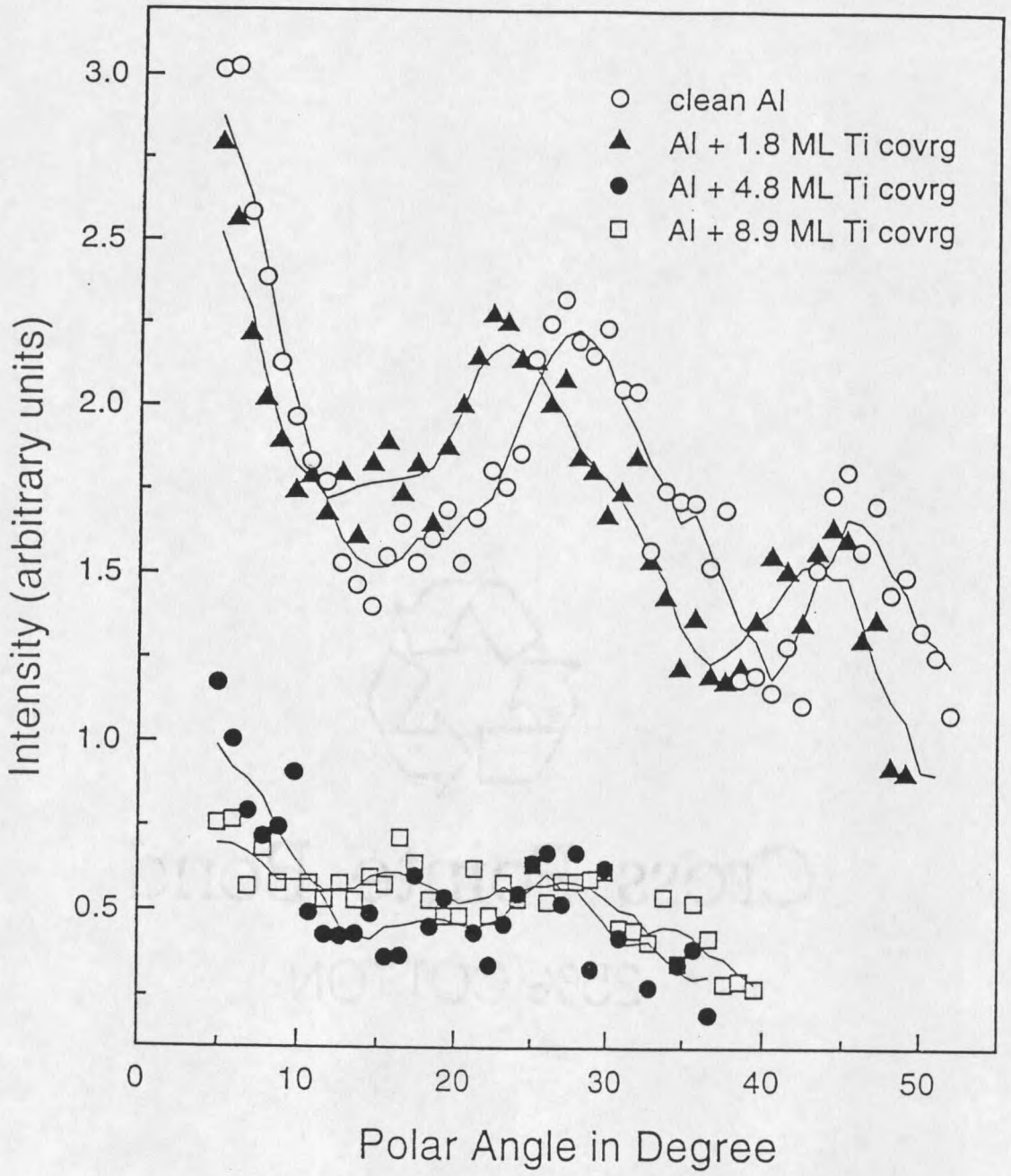

Figure 17: Polar angle scans of the Al 2p peak area in the [110] substrate azimuth for different coverages of Ti on Al (110)

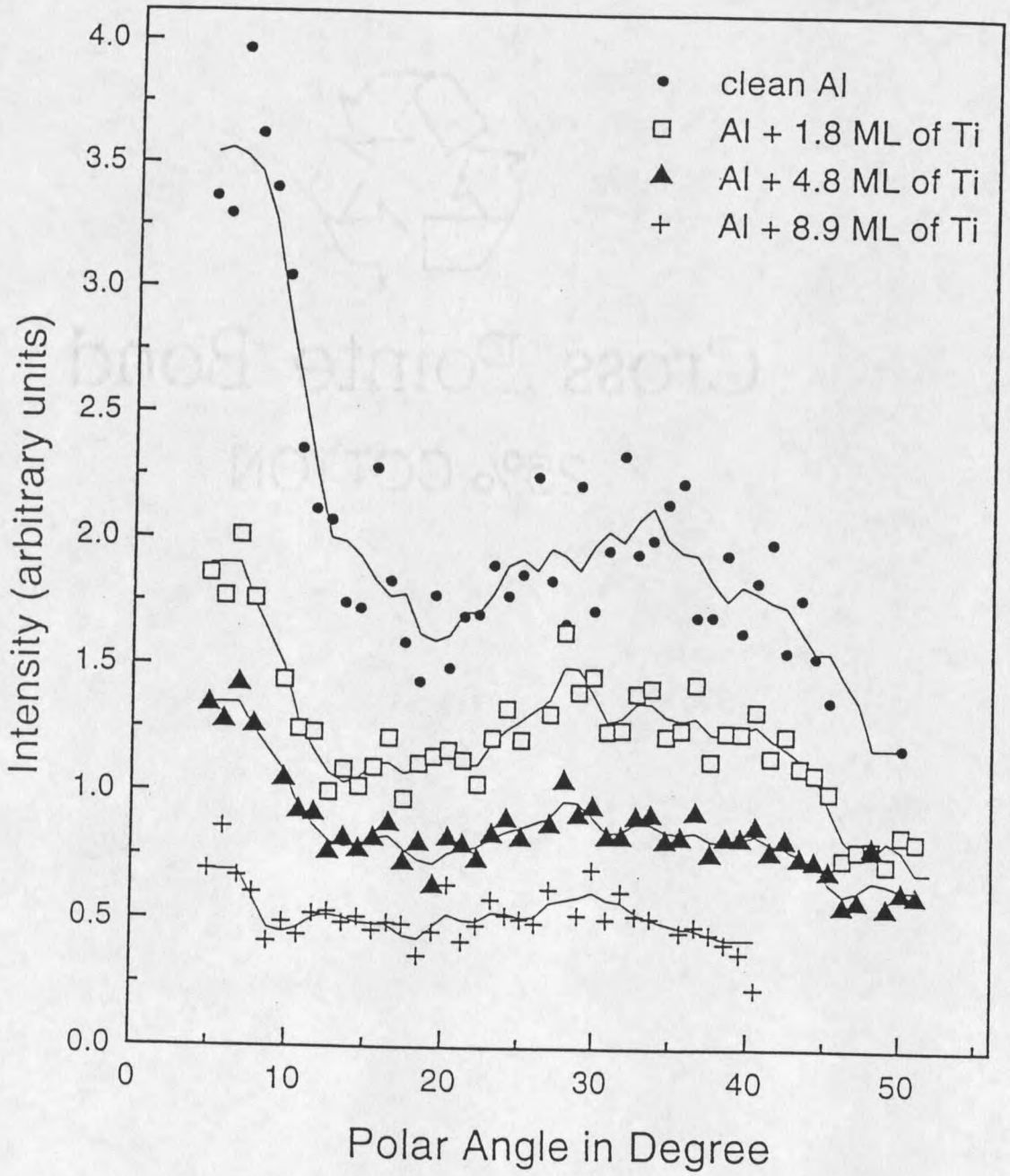

Figure 18: Polar angle scans of the Al 2p peak area in the ⟨100⟩ substrate azimuth for different coverages of Ti on Al(110)

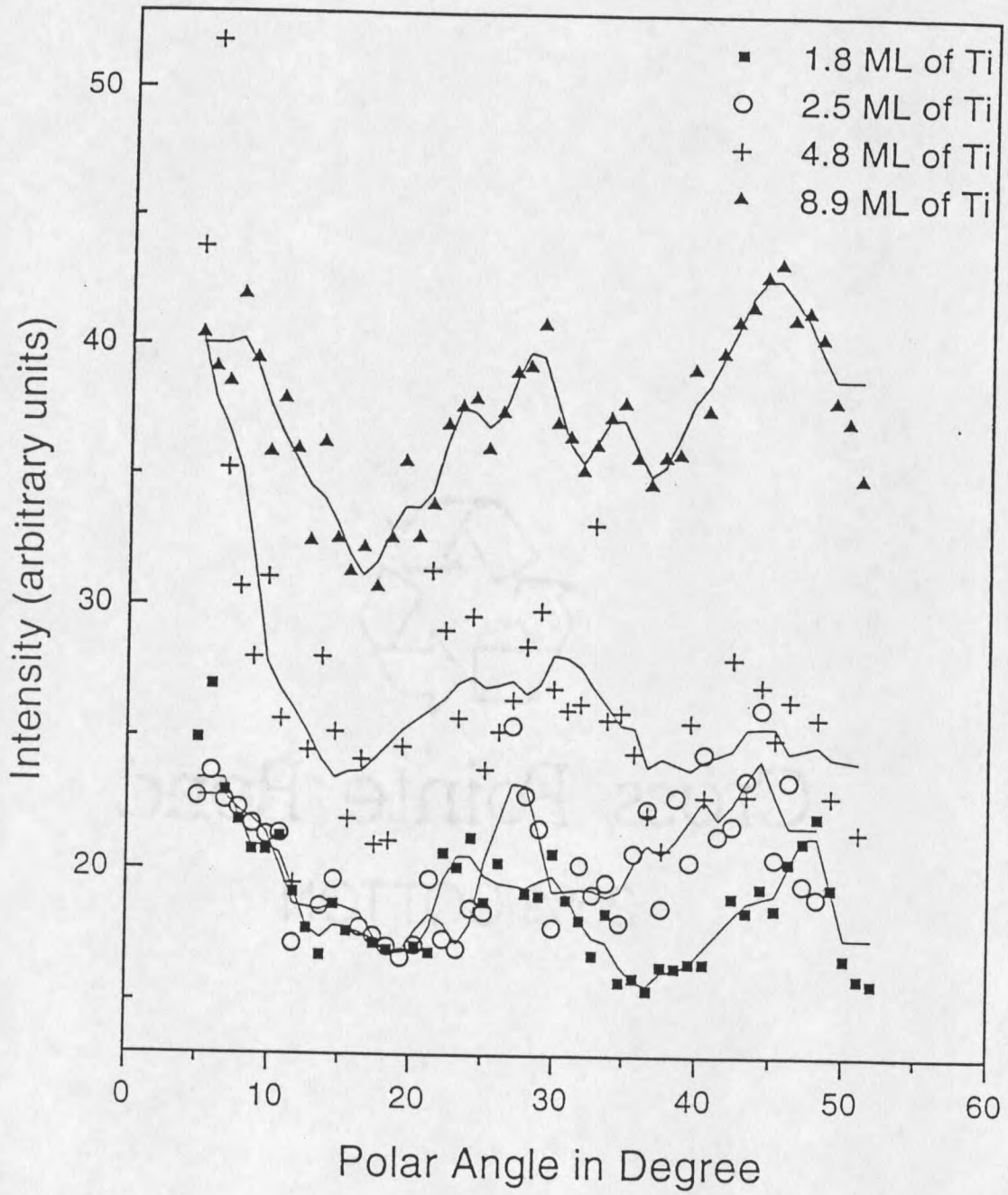

Figure 19: Polar angle scans of the Ti $2p_{\frac{1}{2}}$, $2p_{\frac{3}{2}}$ combined peak area in the ⟨110⟩ substrate azimuth for different coverages of Ti on Al(110)

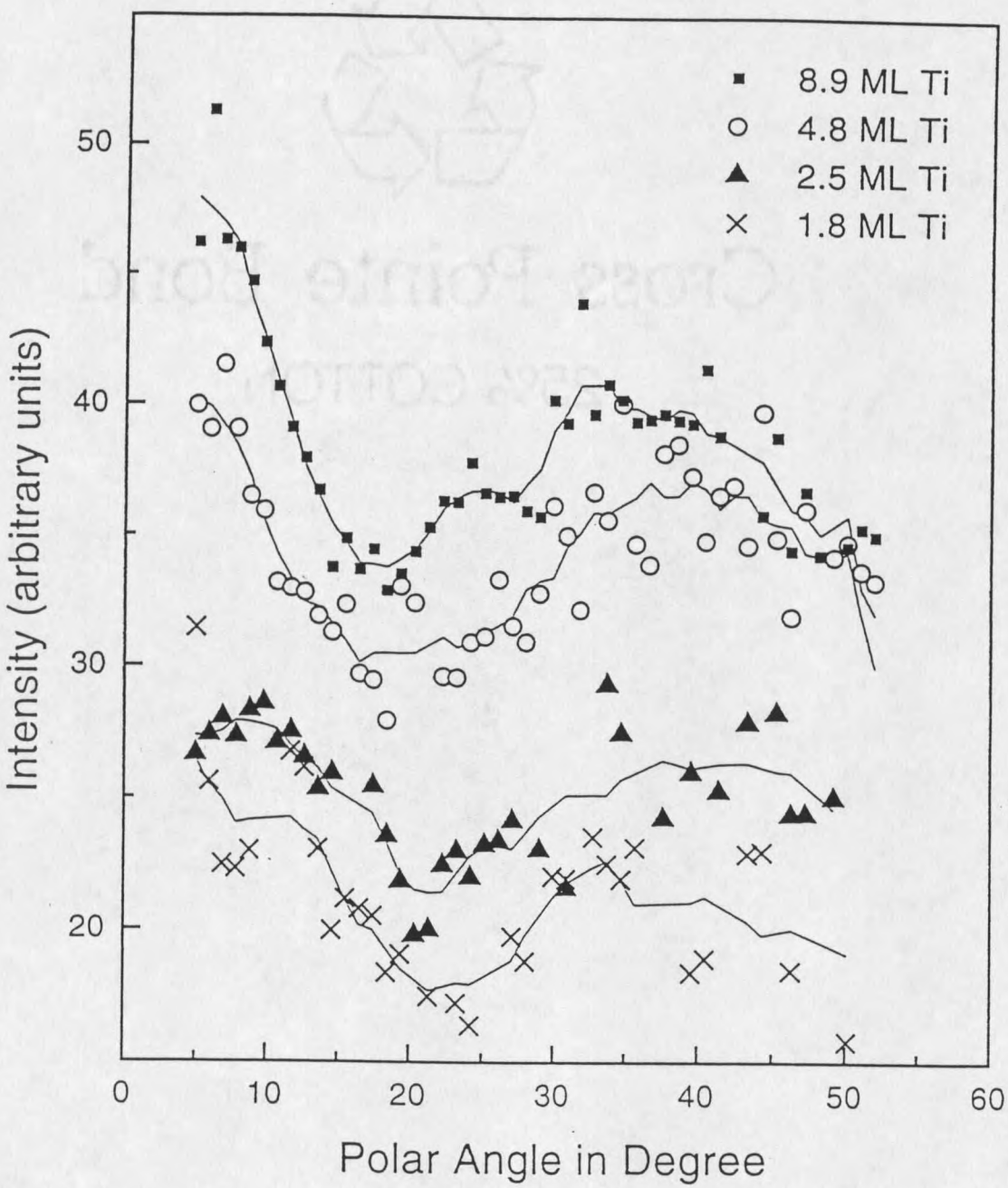

Figure 20: Polar angle scans of the Ti $2p_{\frac{1}{2}}$, $2p_{\frac{3}{2}}$ combined peak area in the [100] substrate azimuth for different coverages of Ti on Al(110)

Low Energy Electron Diffraction

The five sets of LEED patterns were recorded in a separate experiment. Figure 21 and 22 show LEED patterns for different coverages of Ti and different electron beam energies. The patterns represent the reflections for electron energies between 46.8 eV and 119.4 eV. For higher energies the reflections move closer together.

Figure 21 shows the spots for the lower energy of about 46 eV. The three different pictures represent the patterns for clean Al and two different coverages of 1.9 ML and 5.5 ML. Figure 22 shows the same coverages. The pictures are taken at a higher energy (90 eV). In addition to those three patterns the figure also shows the pattern at a coverage of 8.1 ML and an energy of 119 eV.

The different spots for 46 eV and 86 eV are identified in Figure 23 below. The (0,0) spot is shadowed by the electron gun.

Connecting the spots for opposite azimuths (shown in Figure 23) for the clean Al pattern at 46.8 eV leads to two lines almost perpendicular to one another. The angle is 89^0. This angle changes as more Ti is deposited on the Al substrate. The different angles are shown in the following table. This table also includes the vertical distance between the (1,0) and the $(\bar{1},0)$ spots as well as the horizontal distance between the (0,1) and the $(0,\bar{1})$ spots. The distances are measured on the positive photos of the LEED patterns. They do not represent the distances as shown in Figure 21. The distances are only noted when comparison is possible due to energy.

It should be noted that for the higher energy a pattern is still slightly visible for a coverage of 8.1 ML of Ti, even though the pattern is distorted from its original form. For higher coverage the sharp spots that we see for the clean Al surface smear out

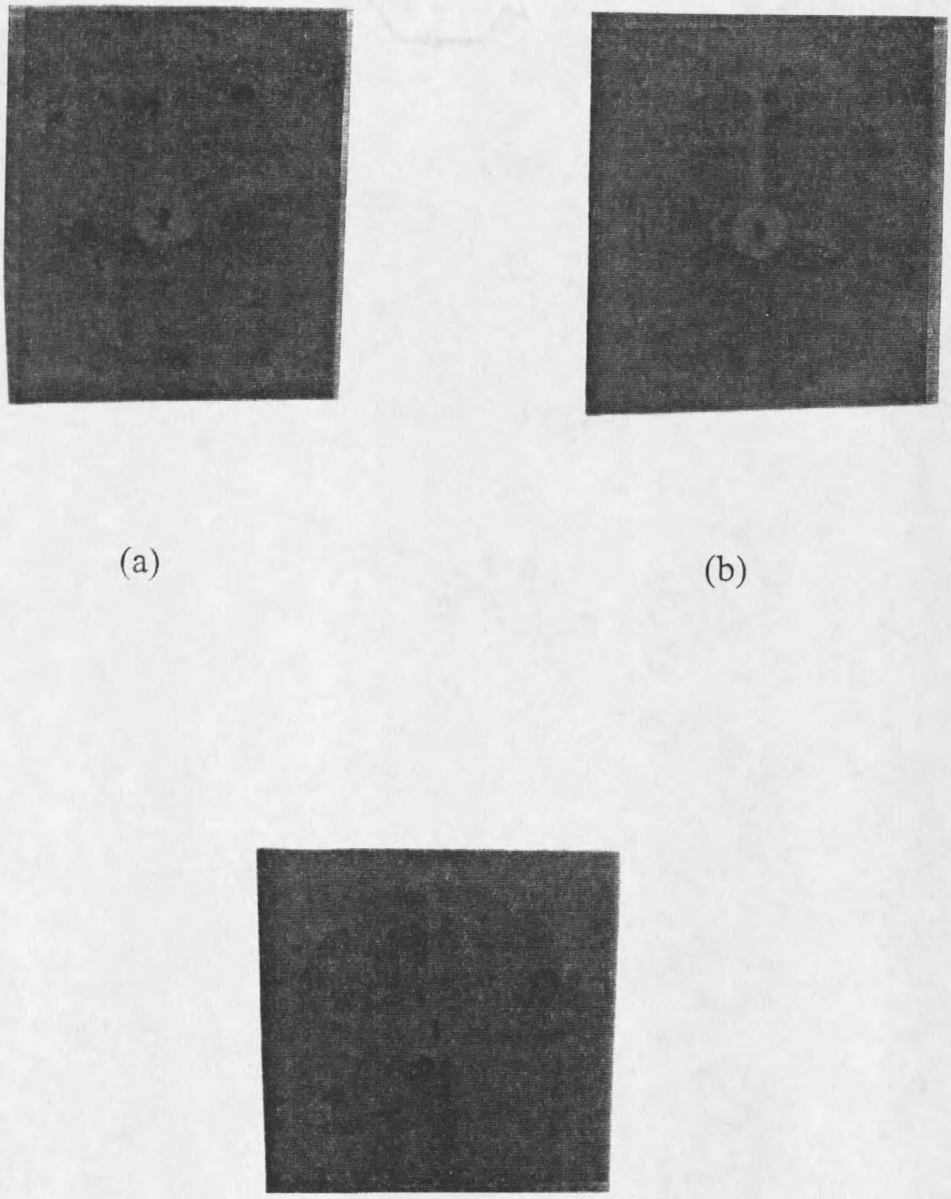

Figure 21: LEED patterns for Al with different coverages of Ti. (a) - (c) show the LEED patterns for energies 46.8 eV, 48.9 eV, and 46.8 eV for clean Al and two different coverages of Ti. (a) clean Al, (b) 1.9 ML of Ti on Al, (c) 5.5 ML of Ti.

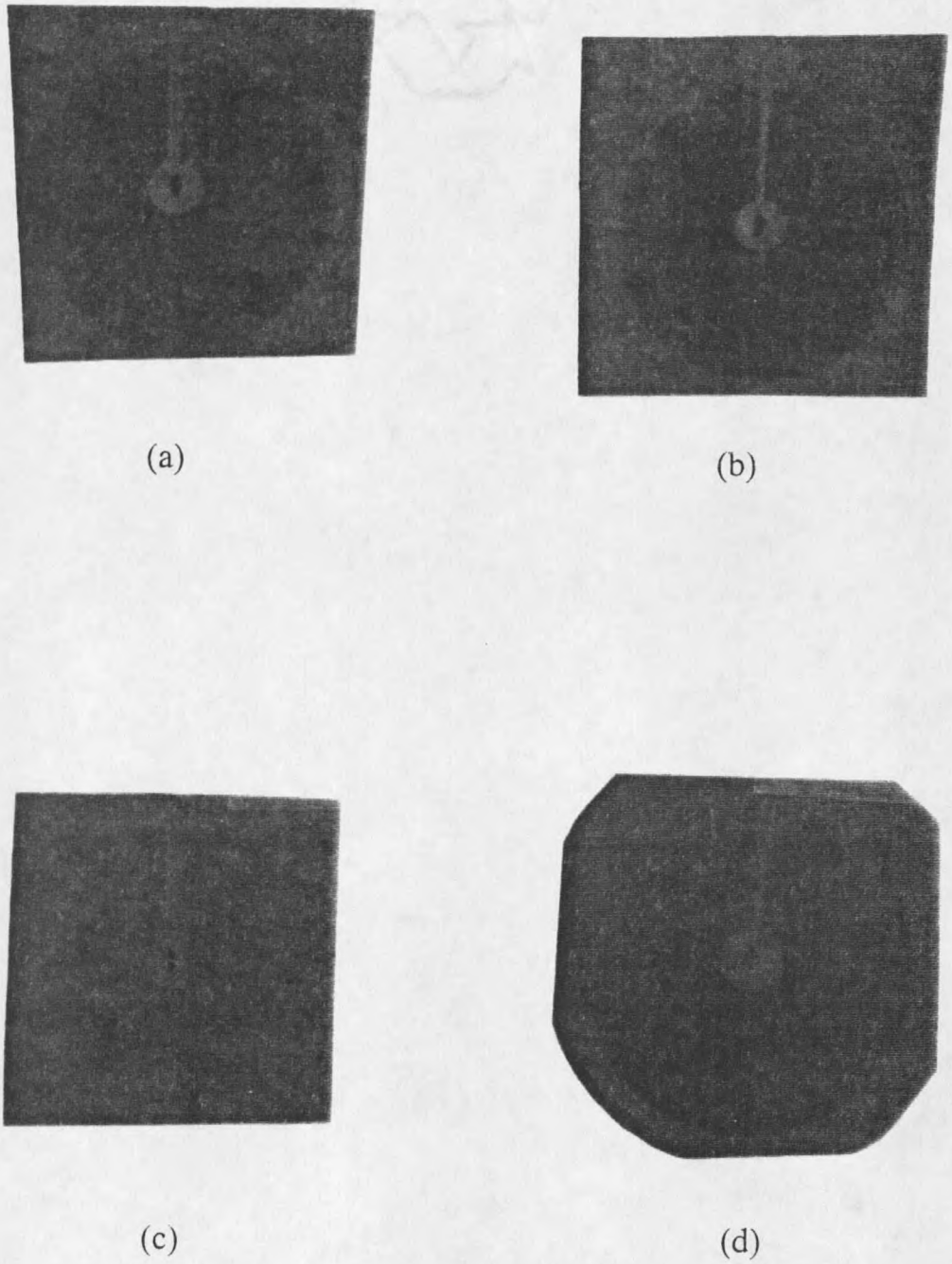

Figure 22: LEED patterns for Al with different coverages of Ti. (a) - (d) show the spots for energies 86.2 eV, 90.4 eV, 86 eV, and 119 eV for clean Al and three different coverages of Ti. (a) clean Al, (b) 1.9 ML of Ti on Al, (c) 5.5 ML of Ti, (d) 8.1 ML of Ti.

Table 2: Angles and distances for LEED spots

Coverage clean Al	**46.8 eV**	**86.2 eV**
angle	89^0	89^0
distances	4.6 cm	3.45 cm
	2.9 cm	4.9 cm
1.9 ML	**48.9 eV**	**90.4 eV**
angle	85^0	85^0
5.5 ML	**46.8 eV**	**86 eV**
angle	70^0	76^0
distances	4.35 cm	3.2 cm
	3 cm	4.75 cm
8.1 ML	-	**119 eV**
angle	-	86^0

and become more diffuse.

Streaks show up in the reflex pattern for 5.5 ML in Figure 22 (c), which enable us to positively identify the orientation of the crystal.

The shadow of the electron gun should not be taken as a reference because the sample was rotated about the azimuth after the Ti deposition.

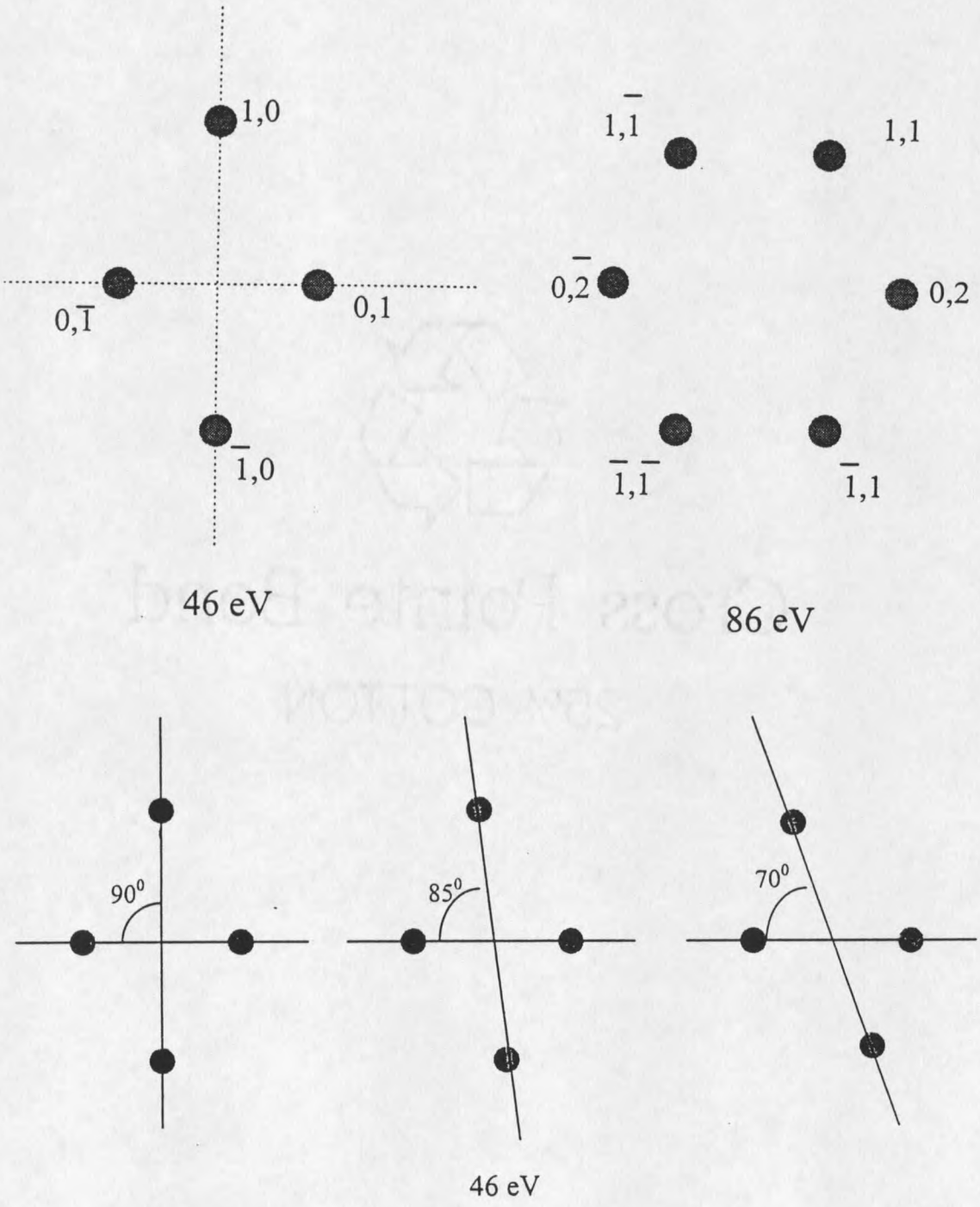

Figure 23: Identification of the LEED spots for 46 eV and 86 eV and the angle between the two axis for clean Al and coverages of 1.9 ML and 5.5 ML.

CHAPTER 5

Interpretation of the Results

X-Ray Photoelectron Diffraction Results

In Figure 24 we show the polar angle distribution of the Al $2p$ intensity for the clean Al surface and for the surface covered with an overlayer of 1.8 ML of Ti. Both curves were taken with the sample in the [110] azimuth. The spectrum for the clean Al shows the distinct *fcc* structure with forward-scattering peaks at 0^0 and 45^0 as expected for the Al bulk. The peak observed at $\approx 26^0$ is due to a combination of the coincidence of two first order constructive interference peaks and an expected peak at 26.5^0 (see Figure 16).

A shift of 2 degrees towards lower angles can be observed in the spectrum of Al covered with 1.8 ML of Ti. According to Egelhoff [8] expansion in an *fcc* lattice is manifested by shifts towards lower angles in the forward scattering peak position at 45^0. The shift of 2^0 corresponds to a lattice expansion of 9%.

Considering that the atoms contributing to forward-scattering peaks are quite near the surface, and that deeper atoms make a somewhat more isotropic contribution due to the defocusing effect, it can be assumed that most of the Al atoms that contribute to the peak at 45^0 lay in the first two layers of the Al substrate [8], [12], [13]. These electrons are scattered by the overlaying Ti atoms.

For a metal surface an imbalance is created in the total force on the lattice plane due to the electron density profile at the surface. That leads to a multilayer lattice relaxation at the surface. For clean Al the top layers become relaxed when forming a

surface. Depositing Ti onto these layers undoes the relaxation. It is reported that for clean Al the first layer contracts by 8.6%, while the second layer expands by 5 %, and the third layer contracts by about 1.6 % [19],[20], leaving an effective contraction of about 5.2%. Upon deposition this contraction is undone, and the corresponding expansion would result in a 1.5^0 shift of the forward-scattering peak toward smaller angles for the Al surface that is covered with 1.8 ML of Ti.

The shift we observed with XPD is almost twice as great as the one observed by Nielsen and coworkers in [20]. It can be argued however that the shift recorded by XPD is mostly due to the relaxation of the first layer and that the contraction of the second and the expansion of the third layer do not contribute equally. The lattice relaxation observed with XPD would therefore be larger because of the exclusion of the canceling effect of the second layer.

Figure 25 shows two diffraction patterns taken from Figure 17. It shows the polar angle dependence of the intensity in the [110] azimuth of the Al $2p$ peak for coverages of 4.8 ML and 8.9 ML of Ti. For these higher coverages of Ti the Al forward-scattering peaks at normal incidence weaken and disappear.

For the thicker films the Ti atoms contribute to a more-or-less isotropic background and lead to defocusing. Defocusing is a consequence of multiple forward-scattering as discussed in an earlier chapter [14]. Figure 17 shows the defocusing effect. For coverages of 4.8 ML and higher the forward-scattering peak at 0^0 is diminished. The peak at 45^0 could not be recorded due to the weak Al $2p$ signal for higher coverages.

The polar angle scan for Al in the [100] azimuth is shown in Figure 18. The spectra for the [100] azimuth show only a forward-scattering peak at normal incidence. The next strongest diffraction peak could be observed at 54^0, but is out of the experimental window for our setup. No new information was obtained from this azimuth. It should

be pointed out however that the first two points of each spectrum are lower then the third. No explanation can be given for such a behavior. It would suggest that the forward-scattering peak at normal incidence (0^0) shifted to higher angles, and we now scan past the normal incidence. However this would further indicate that by rotating the sample to the second azimuth we went off the alignment by 6^0. This is not likely! Therefore no satisfying explanation can be given for such a behavior.

Saleh and coworkers [6] conclude that the Ti film on Al(110) is pseudomorphic and relatively flat. It grows in a layer-by-layer fashion for the first 5 ML. They further conclude that there is a change in structure at 5 ML corresponding to a transformation of the film. Due to the different lattice constants of Al and *fcc* Ti, the Ti overlayer undergoes a change of the interplanar spacing normal to the interface in response to strain in the plane of the interface. This strain remains up to a critical thickness, at which point the strain energy can no longer be accommodated by the lattice and strain relief occurs. Strain can be relieved by mechanisms that include: the introduction of misfit dislocations, the formation of islands by surface diffusion, and interdiffusion of Ti or Al at the interface.

The stable phase of Ti at room temperature is hexagonal closepacked (*hcp*) with $a = 2.95\mathring{A}$ and $c = 4.68\mathring{A}$. An *fcc* phase is not encountered in nature at any temperature. The lattice constant for metastable *fcc* Ti can be calculated from first principle. Moruzzi and Marcus found $a = 4.08\mathring{A}$ [24]. The lattice mismatch between *fcc* Al and *fcc* Ti is thus only 0.75 % (Al: $a = 4.05\mathring{A}$) which makes the pseudomorphic growth of *fcc* Ti likely.

In the next paragraph the growth up to 5 ML is addressed. Figure 26 shows the data set for the XPD scan for the Ti $2p$ peak for a coverage of 1.8 ML of Ti taken from Figure 19.

Figure 26 shows a distinct peak at 48^0 as well as the forward scattering peak

at normal incidence. Later we will discuss why the peak does not occur at exactly 45^0. For the [110] azimuth the peak indicates a structure that gives rise to a forward scattering peak around 45^0. This peak is a strong indicator for the growth of *fcc* Ti on the Al substrate as suggested by Saleh. However it is evident from the schematic shown in Figure 16 that a Ti peak around 45^0 for an *fcc* lattice can only occur after three monolayers of Ti have been deposited. Since the RBS measurements show that only 1.8 ML of Ti have been deposited, we conclude that the Ti does not grow in a layer-by-layer fashion but rather forms islands. The short range order of these islands will then result in the observed peak at 45^0 if the islands have 3 or more monolayers of Ti.

This agrees with the results by Jona and coworkers [21], who report island growth of Ti on Al(110) by the use of Quantitative LEED analysis, which is what is expected considering the surface energies for Ti ($2.570 J/m^2$) and Al ($1.085 J/m^2$) which support the growth of islands.

Figure 27 compares the polar angle scan for Al with that for the Ti overlayer (1.8 ML). Both plots are very similar indicating a similar lattice structure of the bulk Al and the overlaying Ti, although a shift of 2^0 of the 45^0 forward-scattering peak for Ti towards higher angles is noticeable. As shown earlier lattice expansion results in shifts of the forward-scattering peaks towards smaller angles. A shift toward larger angles is the result of a contraction in layer spacing for the epitaxial Ti film on Al. The forward-scattering peak for Ti at 47^0 indicates that the Ti layer spacing is less than that of the underlaying Al lattice, which exhibits a peak at 45^0. A shift of 2^0 would result in a decrease of lattice spacing by 0.2 Å. A decrease in the lattice spacing does not seem physical, since one would expect an increase due to the greater atomic volume of Ti compared to Al ($1.77 \cdot 10^{-23} cm^3/atom$ for Ti compared to $1.66 \cdot 10^{-23} cm^3/atom$ for Al). It is however in agreement with a model presented by Jona and coworkers that

uses contraction of the layer spacing to explain their QLEED data.

One of the models Jona *et.al.* used for low Ti coverages involved a single layer of Ti pseudomorphic to the Al(110) substrate with the atoms located in the positions that would be occupied by Al atoms if the substrate were extended. The layer is pseudomorphic because the interlayer distance was decreased by 0.5 Å. This model gave a better fit to their data than a model of a Ti overlayer with a 0.3 Å larger interlayer distance than that for the bulk Al(110).

Figure 28 shows three different spectra for different coverages of Ti in the [110] azimuth. The spectra are shifted vertically. It is observed that the structure of the overlayer changes for different thicknesses. A similar transformation can be observed in the [100] azimuth as well, as can be seen from Figure 20. We will concentrate on the [110] azimuth however.

A strong forward-scattering peak in the normal direction for a coverage of 4.8 ML is the most prominent feature of Figure 28. However the same scan does not show a peak at 45^0. A structural change must occur in the overlayer if the 45^0 forward-scattering peak disappears.

A simple *fcc* growth where the Ti takes the positions that would be occupied by Al would not explain the disappearance of the 45^0 forward-scattering peak. Let us now assume a structure that starts out as *fcc* and then changes due to strain in the layer. This is indicated in Figure 29.

The figure shows a *face centered* square lattice for the 1^{st} layer. The second and fourth layers are omitted. The third layer is deformed, e.g. the atoms do not sit on top of one another. The fifth layer changes even more in the same direction. If the structure would change the way suggested, the 45^0 forward-scattering peak would not be inside the window that is set for the [110] azimuth. Instead the peak would show up in a different azimuth. Figure 29 indicates that for a coverage of about 5

ML (three atoms) the azimuth is rotated by 20^0 with respect to the original [110] azimuth. This structural change is strongly supported by the LEED data presented in the next section.

However the 45^0 forward-scattering peak reappears in the polar scan for a coverage of 8.9 ML as shown in Figure 30. This peak is now stronger than the peak due to scattering in the normal direction indicating *fcc* short-range order.

The polar angle scans for Ti in the [100] azimuth of Figure 18 do not provide new information. However the strong forward-scattering peak in the normal direction should be noted.

Having established that Ti grows distorted but pseudomorphic on Al(110), one final argument has to be made regarding the interdiffusion of Al into the Ti layer. Neither of the Al scans show an enhancement of the forward-scattering peaks. This indicates that for low coverages of Ti bulk Al does not diffuse substitutionally into the Ti layer. Such a diffusion would show forward-scattering peaks that do not loose their intensity as rapidly as the background does. However, XPD would not detect interdiffusion if the Al diffuses into the layer and the atoms end up at arbitrary places in the lattice of the overlayer.

A pseudomorphic Ti layer on the Al lattice also explains why the peak intensity of the polar angle scan for Al with 1.8 ML of Ti coverage as shown in Figure 24 does not considerably weaken. Even though the Al is now covered, the Ti atoms take over the role of the forward-scatterer for the Al. The nature of the forward scatterer does not matter. However if the Al were covered up by a Ti layer without any structure, the forward-scattering peaks would weaken even for a coverage of 1.8 ML.

Low Energy Electron Diffraction Results

The LEED patterns for different coverages of Ti on Al are shown in Figure 21

and Figure 22. We observe a shift in the LEED patterns for higher coverages with respect to the pattern for clean Al. This shift is most obvious in the LEED patterns of lower energy (46 eV). The angles that are the results of connecting the opposite spots with one another are: 89^0 for clean Al, 84^0 for a 1.9 ML thick Ti layer, and 70^0 for a coverage of 5.5 ML. A 20^0 change in angle corresponds to a distortion of 1.04 Å of one row of atoms with respect to the next, while a 6^0 change indicates a distortion of 0.3 Å. The mechanism of the obvious distortion of the lattice is presented in Figure 31.

The distortion becomes larger with higher coverages until the LEED pattern disappears. At 5.5 ML coverages of Ti we still have a visible LEED pattern indicating long-range order. However the lattice is not simply *fcc* but rather a distorted *fcc* lattice as discussed in the above section. Shearing is visible in Figure 22 (c). This shearing leads to an increase in the atomic distance, which can be observed in a change in distance between the opposite spots on the longer axis. This distance decreases by 7 % from clean Al to a 5.5 ML thick Ti overlayer as shown in Figure 32. The distance of the smaller axis stays nearly constant. The nearest neighbor distance for Al is 2.86 Å. A 7 % increase in the interatomic distance will result in a distance of 3.0 Å. This is in very good agreement with the work by Saleh et.al. [6].

Saleh found the critical thickness at which the pseudomorphic Ti film undergoes a transformation to be 5 ML, using the work by Jesser and Kuhlmann-Wilsdorf [22] and van der Merwe [23]. For this thickness Saleh and coworker found a lattice mismatch of 4.4 %. This mismatch corresponds to an interatomic distance of 2.99 Å.

Assuming the interatomic distance for *fcc* Ti is about 3.0 Å [6], which is close to the nearest-neighbor distance for hexagonal Ti, we suggest that Ti starts out as *fcc* due to the bulk Al and then distorts to reach the natural hexagonal stage.

This growth mode however does not correspond to the channeling data of Saleh

et.al.. A distortion as suggested above for a film thickness of up to five monolayers would uncover bulk Al atoms. But instead Saleh observed shadowing of the substrate Al by the overlaying Ti. A 0.3 Å distortion of one layer with respect to next as we observed for a coverage of 1.9 ML however might well be inside the limits for shadowing if one also considers the growth of islands.

We lose the long-range order for coverages of 8.1 ML. Only a very diffuse LEED pattern is visible for this coverage at an energy of 119 eV, as can be seen from Figure 22. The presence of forward-scattering peaks for these coverages suggests that we lost only the long range order but still maintain a short-range order. This is an indication for the growth of islands above 5 ML – islands large enough to cause forward scattering but too small to exhibit long-range order. This is consistent with the interpretation of the results by Saleh and coworkers, who could account for all their observations by assuming the formation of islands for coverages higher than 5 ML.

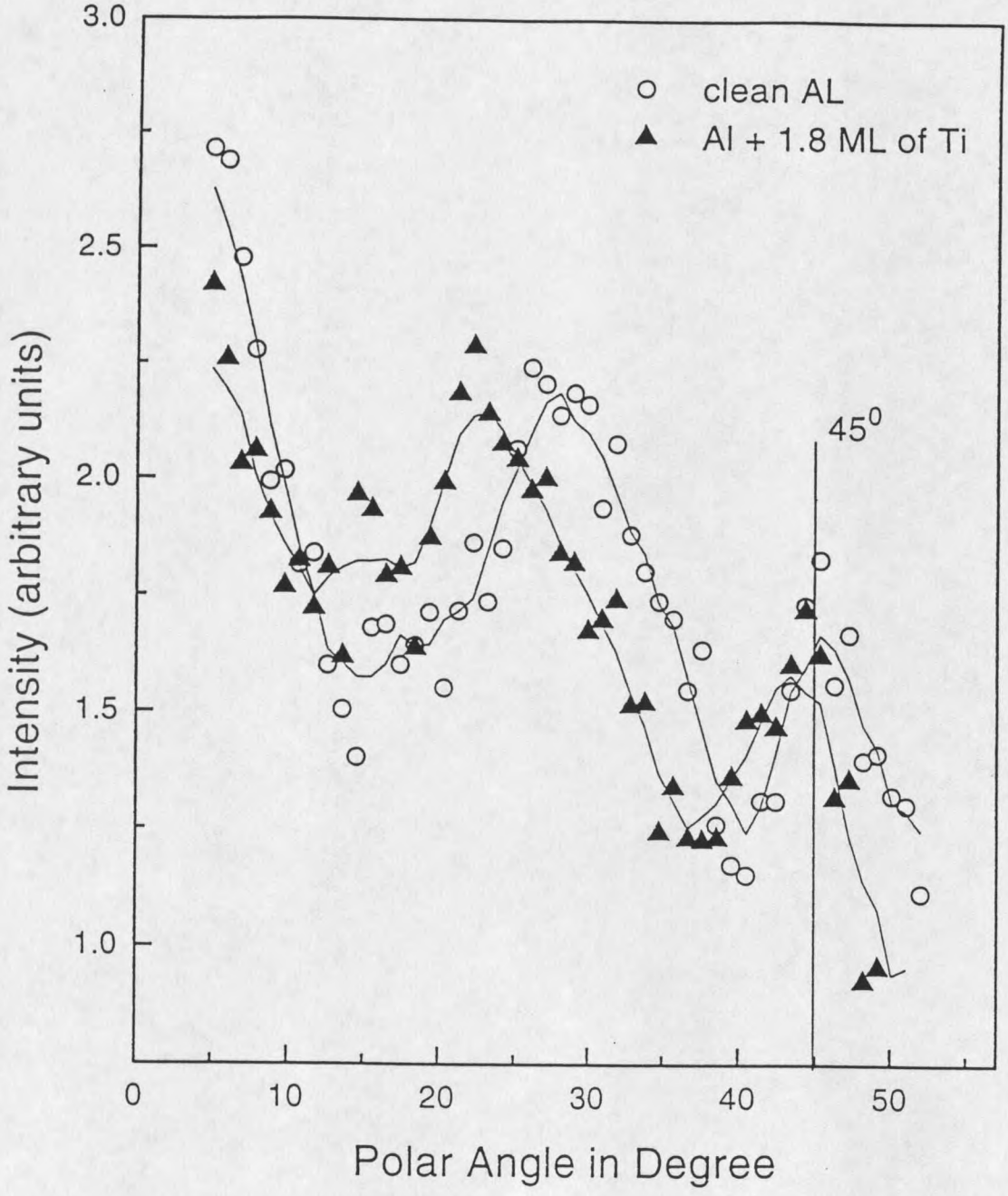

Figure 24: Polar angle distribution of the Al $2p$ intensity for clean Al and with a coverage of 1.8 ML of Ti on Al(110) in the [110] azimuth

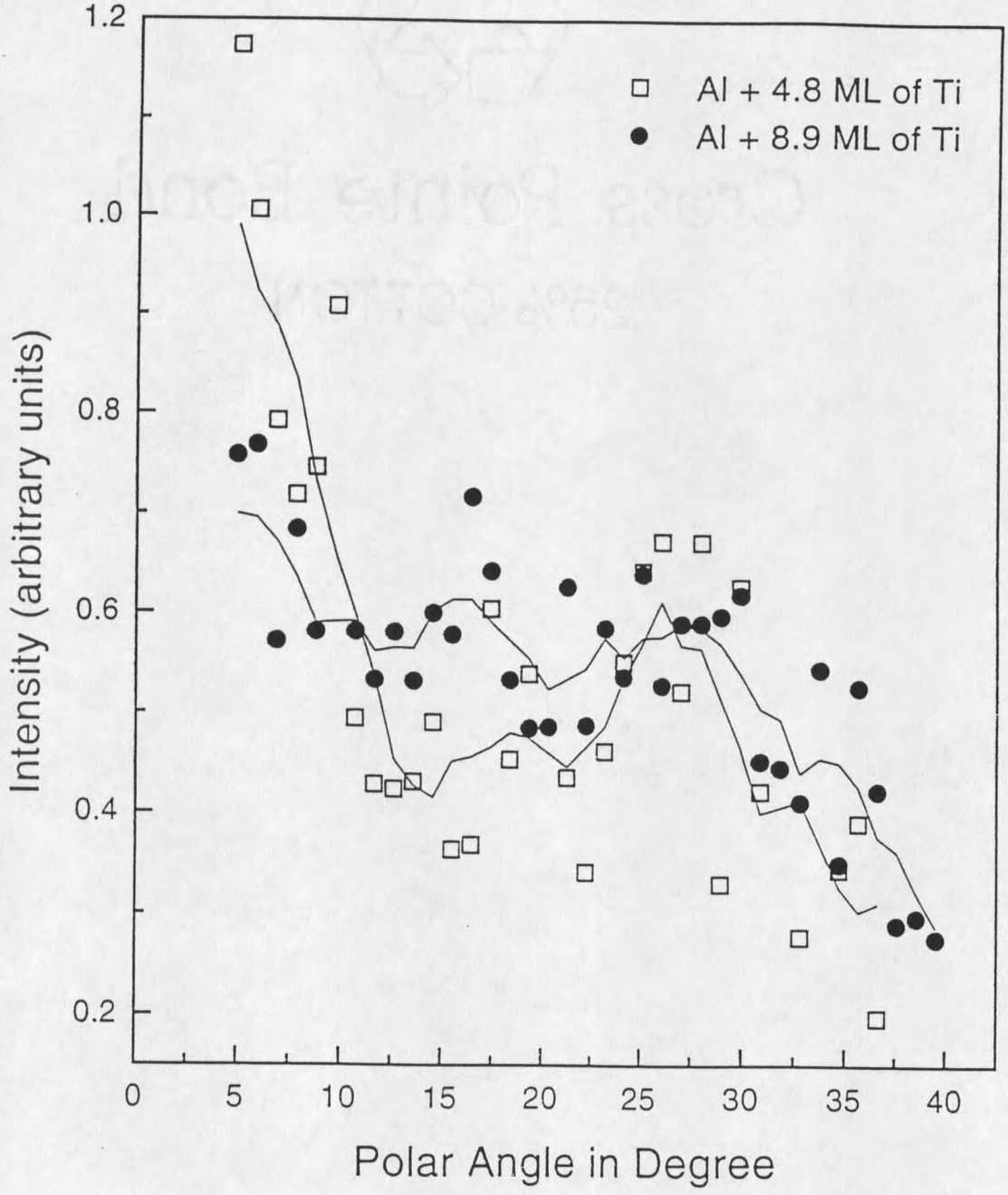

Figure 25: Polar angle distribution of the Al $2p$ intensity for Al for 4.8 ML and 8.9 ML coverages of Ti in the [110] azimuth

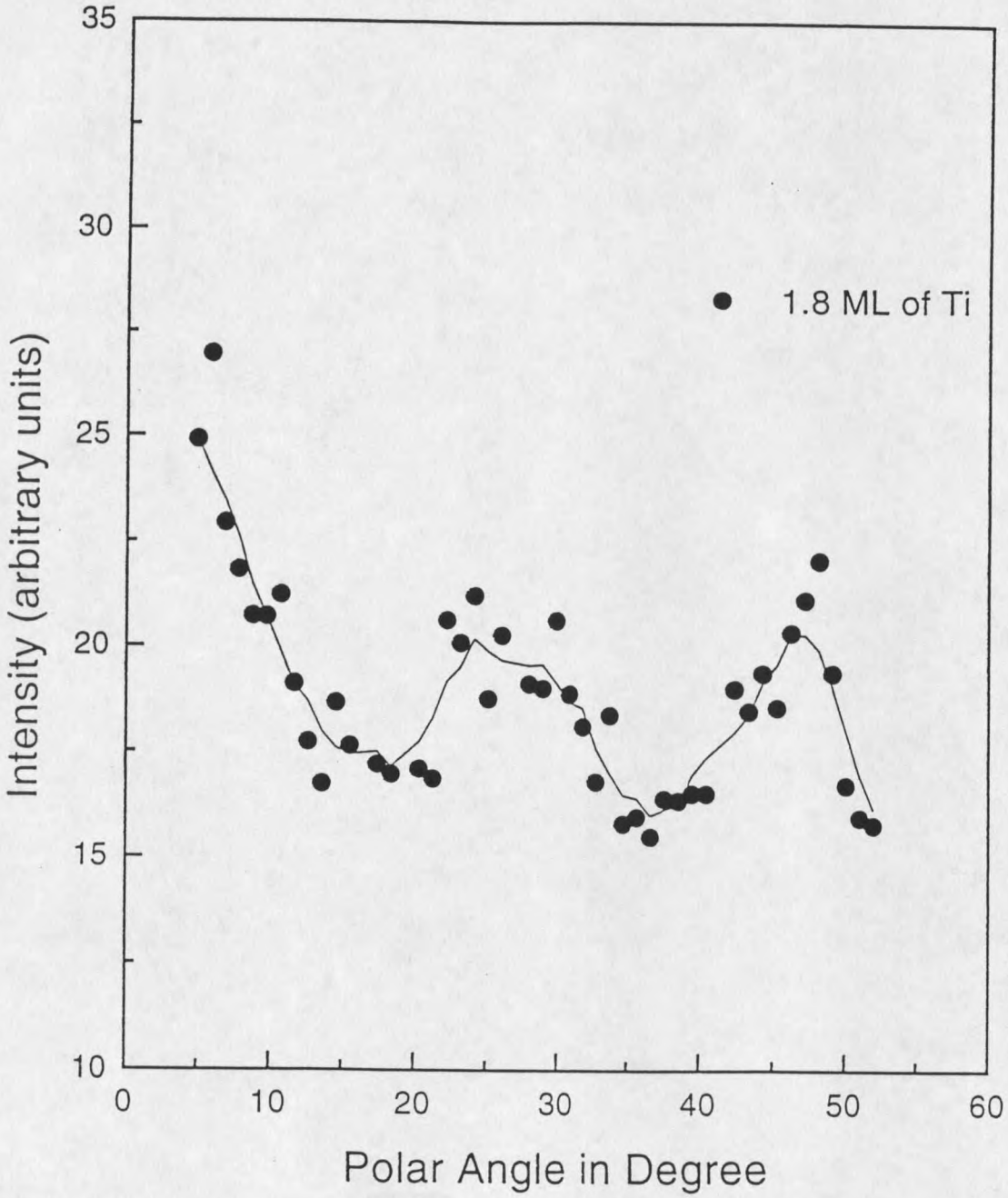

Figure 26: Polar scan for the Ti $2p$ for a coverage of 1.8 ML of Ti on Al(110) in the [110] azimuth.

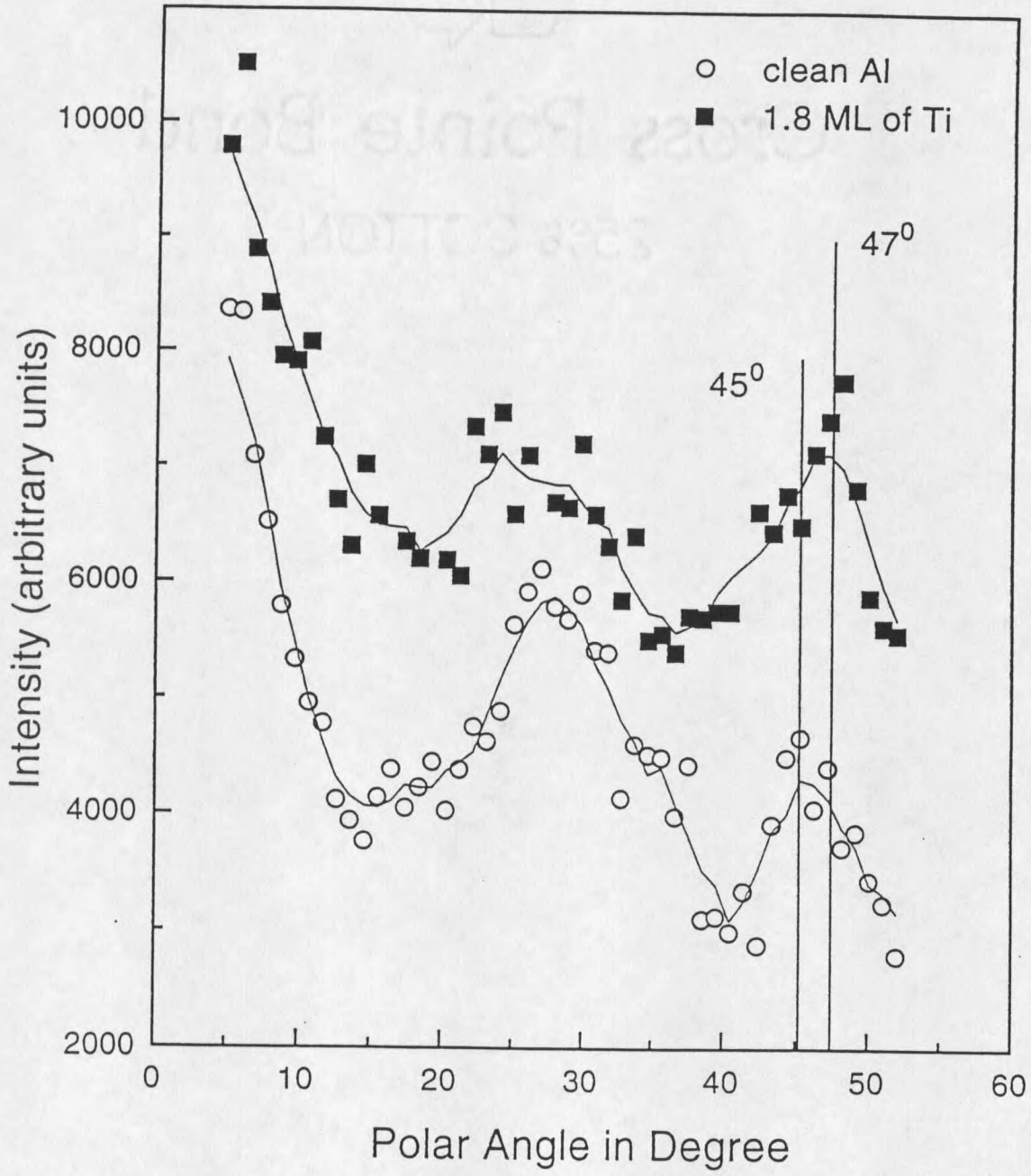

Figure 27: Comparison between the Ti polar scan for 1.8 ML and the Al scan for clean Al in the [110] azimuth.

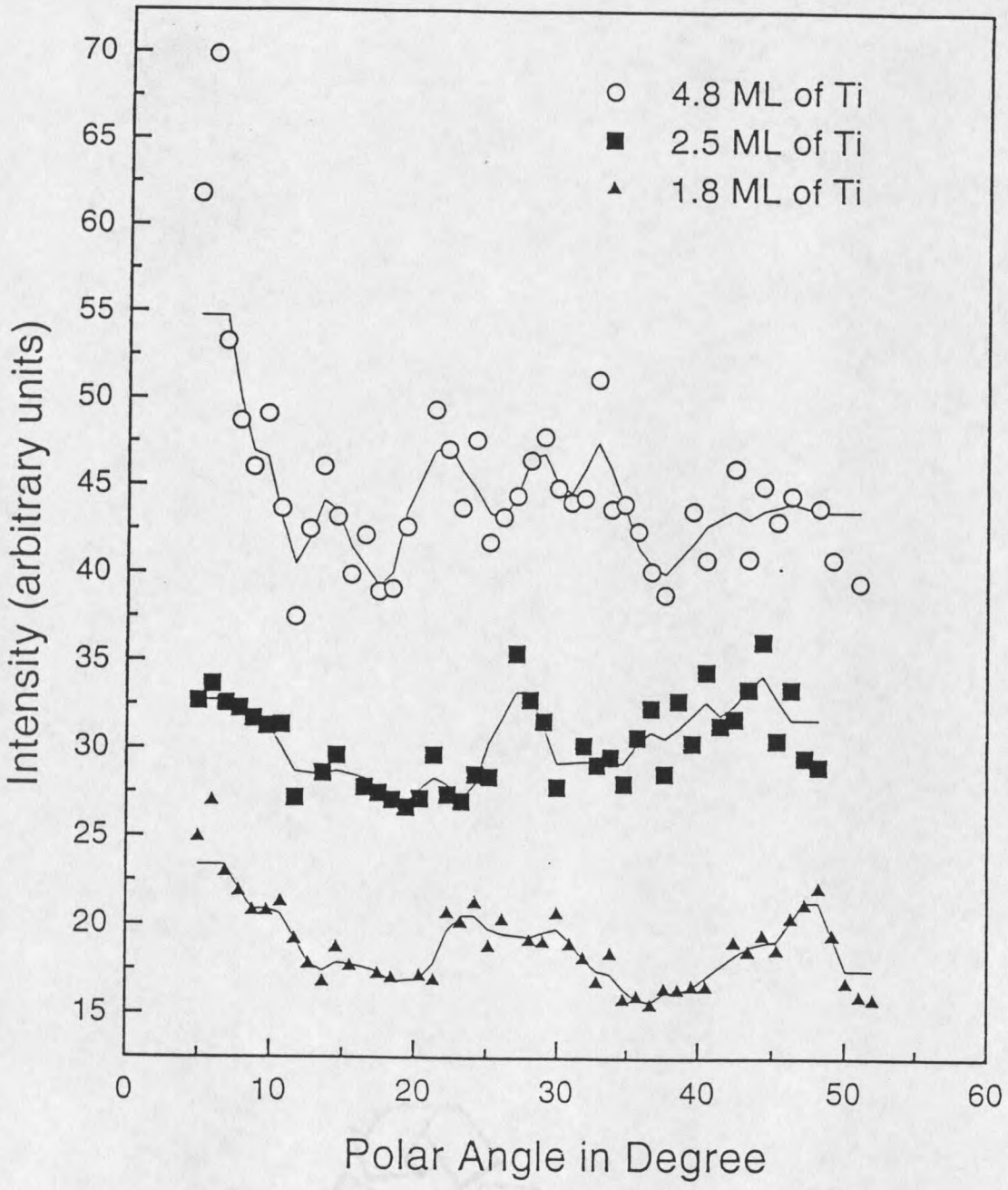

Figure 28: Polar scan for the Ti $2p$ for a coverage of 1.8, 2.5, and 4.8 ML of Ti on Al(110) in the [110] azimuth.

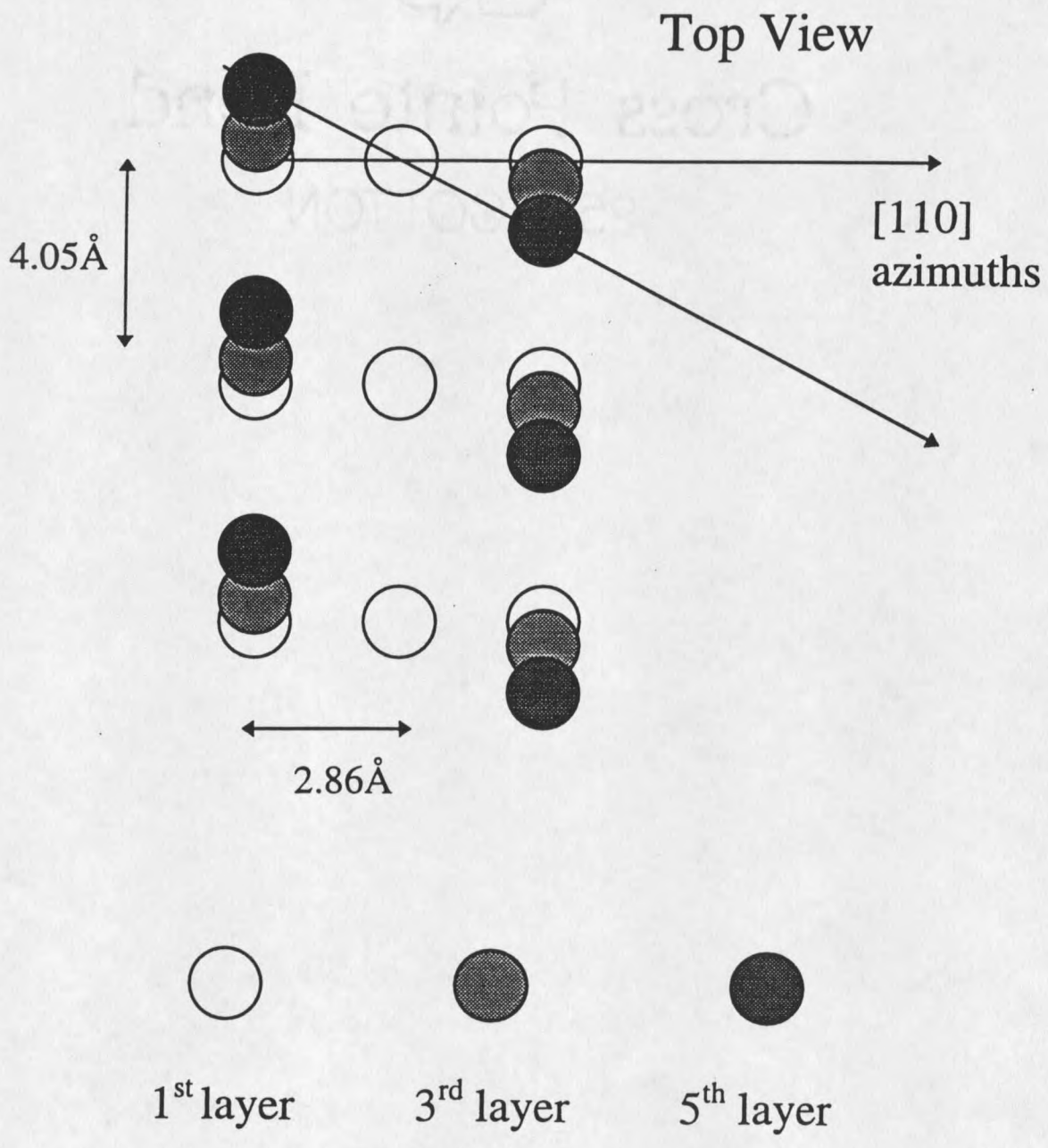

Figure 29: *fcc* lattice structure indicating a change due to strain

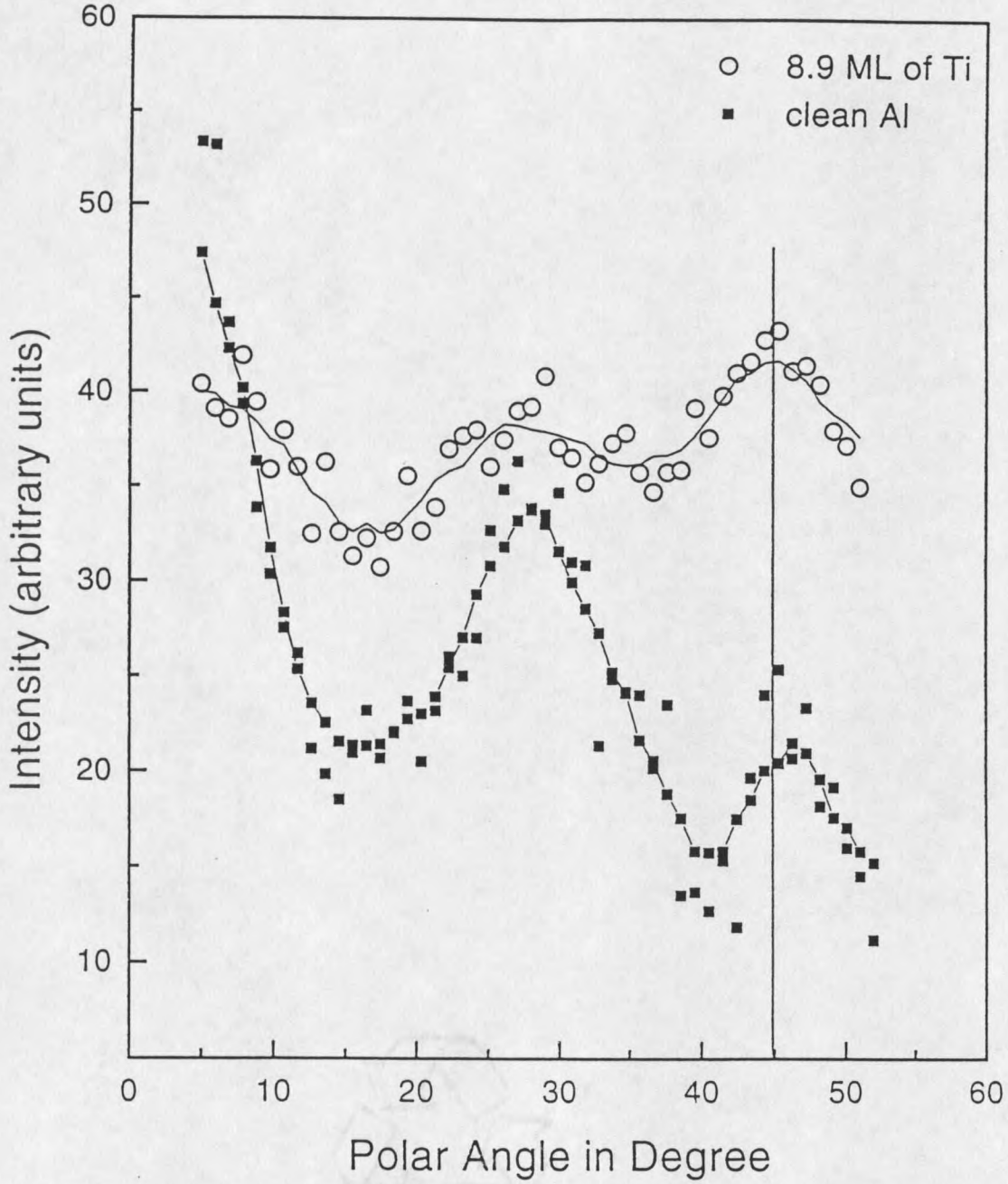

Figure 30: Polar angle scans for Al and Ti in the [110] azimuth. The diffraction pattern for Ti is taken for 8.9 ML of Ti on Al. The Al pattern is shifted to allow a better comparison.

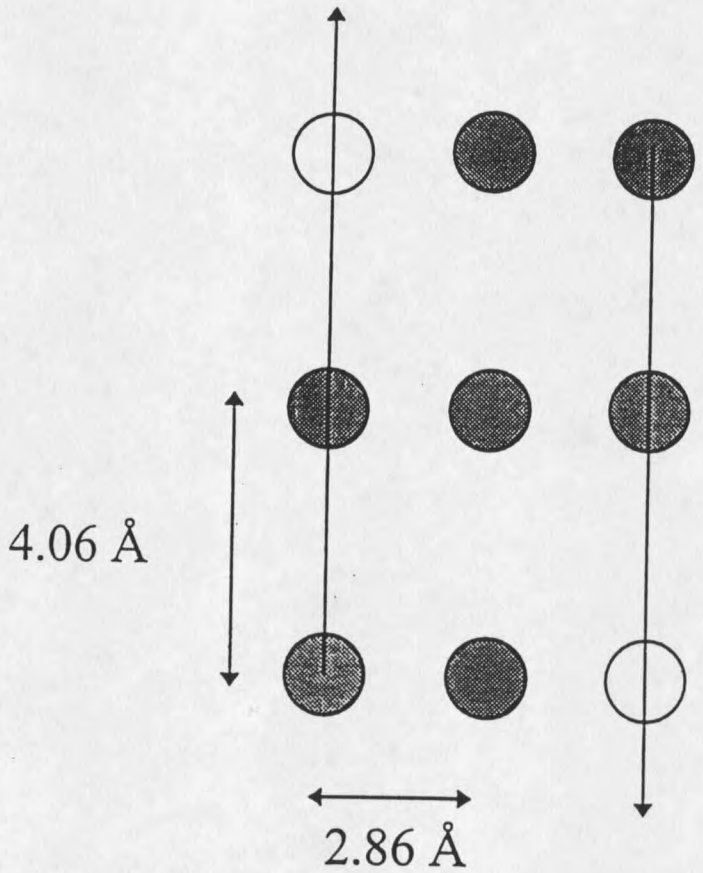

Figure 31: Mechanism of the lattice distortion that can cause the observed LEED patterns.

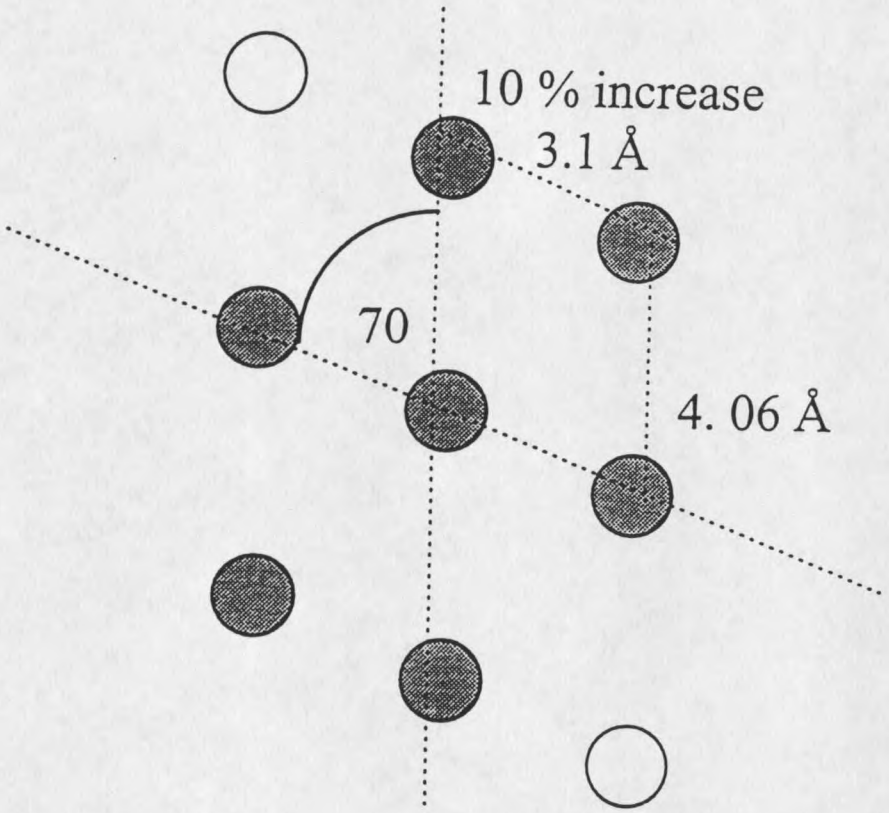

Figure 32: Distortion of the LEED spots. Indicated are the changes in angles and distances.

CHAPTER 6

Conclusion

In this thesis we investigated the growth of Ti on the (110) surface of Al using XPD and LEED as our main techniques. We observed a change in interlayer distance for Al of 9% due to an expansion of the top layers after deposition of a 1.8 monolayers of Ti. We could verify that the Ti film grows pseudomorphic on Al(110), but that it grows by forming islands. Our XPD data led us to assume that for the Ti in the overlayer the layer spacing is less than that of the bulk Al. The layer spacing decreases by 0.28 Å.

For coverages above 3 ML a structural change occurs due to strain in the layer. The structure is still *fcc* but is distorted towards a hexagonal closepacked lattice. Furthermore we found that even for a coverage of 8.9 ML the overlayer still exhibits short range order as face-centered-cubic but that no long-range order is present.

Interdiffusion of Al into the Ti overlayer can be ruled out as a strain relief process due to the absence of a strong forward-scattering peak for Al after higher coverages of Ti. The peaks disappear according to the defocusing effect.

Further LEED measurements could lead to more insight in the mechanism of the distortion of the overlayer. Once the angle for a certain coverage is established, XPD measurements in this azimuth could then in turn verify that the overlayer is still *fcc*. These experiments should be coupled with HEIS measurements for consistency.

BIBLIOGRAPHY

[1] H. Li, B.P. Tonner, Surf. Sci. 237, 141 (1990).

[2] H. Li, B.P. Tonner, Phys. Rev. B 40, 10241 (1989).

[3] M. Hansen: *Constitution of Binary Alloys* McGraw-Hill, New York, 1958

[4] R.E. Vitturo, et. al., Appl. Phys. Lett., 52, 2052 (1988).

[5] A.A. Saleh: *A new phase of Titanium on Aluminum surfaces: Epitaxial growth and hydrogen uptake properties* Dissertation Thesis, Montana State University (1994).

[6] A. Saleh, V. Shutthanandan, and R.J. Smith: *Observations of ultrathin metastable fcc Ti films on Al(110) surfaces,* Phys. Rev. B (15 Feb., 1994).

[7] V.S. Shutthanandan: *Experimental and theoretical studies of reaction and growth of ultrathin Ni and Pd films on Al single crystal surfaces* Dissertation Thesis, Montana State University (1994)

[8] W.F. Egelhoff, Jr.: *X-Ray Photoelectron and Auger Electron Forward Scattering: A Structural Diagnostic for Epitaxial Thin Films,* Springer-Verlag, Berlin, (1994).

[9] S.A. Chambers: *Epitaxial film crystallography by high-energy Auger and X-ray photoelectron diffraction,* Advances in Physics, 40, No.4, 357 (1991).

[10] W. Chu, J.W. Mayer, M.A. Nicolet: *Bachscattering Spectroscopy* Academic Press (1978)

[11] L.C. Feldman, J.W. Mayer: *Fundamentals of Surface and Thin Fil Analysis* North-Holland (1986)

[12] W.F. Egelhoff, Jr., Phys. Rev. B 30, 1052 (1984).

[13] W.F. Egelhoff, Jr., Vav. Sci. Technol. A 4, 758 (1986).

[14] S.Y. Tong, H.C. Poon, D.R. Snider, Phys. Rev. B 32, 2096 (1985).

[15] J. Osterwalder, T. Gerber, S. Hüfner, L. Schlapbach: *Photoelectron diffraction from core levels and plasmon-loss peaks of aluminum* Phys. Rev. B 41, 18, (15 June 1990).

[16] P. Aebi, M. Erbudak: *Imaging of surfaces by means of secondary electrons* Surf. Sci. 285, 275 – 281, (1993)

[17] R.M. Stern, H. Taub, Phys. Rev. Lett. 20 (1968) 1240

[18] D.A. Shirley, Phys. Rev. B, 5, 4709 (1972)

[19] A.G. Eguiluz: *Lattice relaxation at an aluminum surface: Self-consistent linear-electronic-response approach* Phys. Rev. B, 35, 11, (15 April 1987)

[20] H.B. Nielsen, J.N. Andersen,L. Petersen, D.L. Adams, J. Phys. C 15, L1113 (1982) *ibid.* 17, 173, (1984)

[21] S.K. Kim, F. Jona, P.M. Marcus: *Metastability of face-centered-cubic titanium*

[22] W.A. Jesser, D. Kuhlmann-Wilsdorf, Phys. Status Solidi 19, 95 (1967).

[23] J.H. Merwe, J. Appl. Phys. 34, 117, (1963) J. Appl. Phys. 34, 117, (1963)

[24] V.L. Moruzzi, P.M. Marcus: *Handbook of Magnetic Materials*, North Holland, New York (1993)

MONTANA STATE UNIVERSITY LIBRARIES
3 1762 10242198 7